

Northumbria Research Link

Citation: Peng, Hua-Feng, Luo, J. K. and Fu, Yong Qing (2018) ZnO Thin Films and Nanostructures for Acoustic Wave-Based Microfluidic and Sensing Applications. In: Functional Materials and Electronics. Apple Academic Press, Oakville, pp. 195-262. ISBN 9781771886109

Published by: Apple Academic Press

URL:

This version was downloaded from Northumbria Research Link:
<http://nrl.northumbria.ac.uk/id/eprint/32882/>

Northumbria University has developed Northumbria Research Link (NRL) to enable users to access the University's research output. Copyright © and moral rights for items on NRL are retained by the individual author(s) and/or other copyright owners. Single copies of full items can be reproduced, displayed or performed, and given to third parties in any format or medium for personal research or study, educational, or not-for-profit purposes without prior permission or charge, provided the authors, title and full bibliographic details are given, as well as a hyperlink and/or URL to the original metadata page. The content must not be changed in any way. Full items must not be sold commercially in any format or medium without formal permission of the copyright holder. The full policy is available online: <http://nrl.northumbria.ac.uk/policies.html>

This document may differ from the final, published version of the research and has been made available online in accordance with publisher policies. To read and/or cite from the published version of the research, please visit the publisher's website (a subscription may be required.)



**Northumbria
University**
NEWCASTLE



UniversityLibrary

CHAPTER 5

ZNO THIN FILMS AND NANOSTRUCTURES FOR ACOUSTIC WAVE-BASED MICROFLUIDIC AND SENSING APPLICATIONS

HUA-FENG PANG^{1,2}, J. K. LUO³, and Y. Q. FU^{2*}

¹Department of Applied Physics, School of Science, Xi'an University of Science and Technology, Xi'an, PR China

²Faculty of Engineering and Environment, Northumbria University, Newcastle upon Tyne NE1 8ST, United Kingdom

³Centre for Material Research and Innovation, University of Bolton, Deane Road, Bolton BL3 5AB, United Kingdom

**Corresponding author. E-mail: Richard.fu@northumbria.ac.uk*

CONTENTS

Abstract.....	196
5.1 Introduction.....	196
5.2 ZnO Thin Films and Nanostructures.....	198
5.3 Engineering and Development of ZnO-Based Devices.....	221
5.4 ZnO Acoustic Wave Devices	223
5.5 ZnO-Based Acoustic Wave Microfluidics	230
5.6 ZnO Thin Films and Nanostructures for Sensing Application.....	239
5.7 Summary and Future Trends.....	249
Acknowledgments.....	250
Keywords	251
References.....	251

ABSTRACT

Progress in ZnO thin films and nanostructures for the acoustic wave microfluidic and sensing applications are reviewed in this chapter. ZnO thin films with good piezoelectric properties possess large electromechanical coupling coefficients and can be fabricated for the surface acoustic wave (SAW) and film-bulk acoustic resonator (FBAR) devices with a good acoustic performance. The SAWs can be excited to mix, stream, pump, eject, and atomize the liquid, and precision sensing can be performed using SAWs and FBARs. Therefore, the ZnO SAW devices are attractive to be integrated into a lab-on-chip system where the SAWs can transport bio-fluids to the desired area, mix the extracted DNA or proteins, and detect the changes of the signals using SAWs or FBARs. The ZnO SAW and FBAR devices in combination with different sensing layers could also be used to successfully detect gas, UV light, and biochemicals with remarkable sensitivities.

5.1 INTRODUCTION

Zinc oxide (ZnO) is a binary compound via a covalent bonding between the transition-metal zinc atom and oxygen atom. ZnO thin films and nanostructures are multifunctional materials, which have attracted much attention from as early as 1930s until today due to various fundamental electronic, chemical, physical, and optical properties and applications [1–3]. In recent years, the development of new growth technologies of ZnO thin films and nanostructures and their new applications has renewed lots of interest on obtaining the high-quality thin films and single crystals [4–7], and further investigation of their growth mechanism, band structures, excitons, and deep centers in luminescence, nonlinear optics, and UV lasing [8,9]. With in-depth understanding of the semiconducting, optical, electronic, piezoelectric, and pyroelectric properties, ZnO has now been widely applied for microfluidics, optoelectronics, piezotronics, sensors, solar cell, and actuators [10–12]. These immense applications also have boosted the extensive researches on the fundamentals and growth techniques of the ZnO-based materials.

Microfluidics is focused as one of the important applications, which is an interdisciplinary science of controlling and manipulating the flow of liquids typically at micron and submicron dimensions in a miniaturized system and the corresponding technologies for such systems. This multidisciplinary technology is comprehensively based on physics, nanotechnology, biotechnology, chemistry, and electronic engineering. Microfluidics is crucial to

the developments of the inkjet print-heads, DNA chips, and lab-on-a-chip (LOC) technologies [13]. The typical flow of liquid with very small volume is conveniently handled through generating, transporting, separating, mixing, nebulizing, and heating in the microfluidic system [14]. This endows the microfluidics with distinctive advantages such as low fluidic volume consumption, high-throughput, compactness, high sensitivity, fast response, high-speed processing, and low energy consumption [12,14–17]. Therefore, a rapid increase in the development of new methods to modulate fluid flow at microscale has been supported with the urgent needs from healthcare, medical research, life science, drug-development sectors. However, the microscale fluids obviously differ with the flow features of the conventional large fluid with macro scale due to differences in their surface tension, energy dissipation, and fluidic resistance, etc. Some physical and chemical effects and phenomena become dominant at a microscale level, such as capillary forces, surface roughness and undesired chemical interactions. These may be difficult to accurately predict and design, which results that the fabrication processes of these microsystems is more complex and difficult than those for the conventional ones. Various technologies, including eletrokinetics, electrowetting, and acoustic wave technology, etc. have been integrated into the LOC microfluidic systems [15], which are used to overcome above problems. The planar chip which combines the surface acoustic wave (SAW) technique into the droplet microfluidics is more efficient and attractive than the conventional channel-based chip [16]. Therefore, the SAW microfluidics become an important and fundamental field of the enormous researches on the programmable microfluidic chip [17,18].

Acoustic wave is generated from the piezoelectric materials using electric fields applied onto the electrodes of the acoustic wave device. The features of the acoustic waves are determined by the propagation ways because of the piezoelectricity and the boundaries in the materials. Different acoustic waves can be categorized into SAW, bulk acoustic wave, shear-horizontal wave, acoustic plate mode wave, Love wave and Lamb wave, etc. [19]. The SAW techniques offer simpler and more compact devices without moving parts when the acoustic wave is designed to interact with the fluids, and SAW microfluidics has been extensively studied in recent years because of considerable interest and developments on SAW technology in the past decades. The microfluidic coupling among the fluid, acoustic wave, and microstructure is modulated to be more efficient, reliable, and controllable for the integrated LOC microfluidic device [14]. Compared with bulk piezoelectric materials (e.g., quartz, lithium tantalite, and lithium niobate), thin films (e.g., ZnO, aluminum nitride, and lead zirconium titanate or PZT) have

advantages of simple, inexpensive and large-scale production, and flexible integration with the microfluidic structures and controller circuits. Therefore, ZnO-based microfluidics is recently presented as one of the key the main applications for ZnO thin films and nanostructures.

A sensor is a device or instrument that converts the physical/chemical/electrical/mechanical quantities into visible or readable signals. It normally consists of three units, including the input port, sensing unit, and output port, with a functional relationship between the input and output quantities in a form of electrical or optical signals. The sensor always appears as a probe device that widely exists around our world, covering natural sensors in living organisms such as eye, nose, and ear, and the artificial sensors including biochemical sensors, gas sensors, physical sensors such as humidity and temperature sensors, pressure sensor, and viscometers [20,21]. The sensor technologies have made a remarkable leap in the last a few decades owing to the development of micro-electromechanical systems (MEMS) in micro-electronic engineering [20]. This allows multiple sensors to be manufactured at micro or nanoscale as microsensors or nanosensor, which can reach a significantly higher selectivity and sensitivity compared with the macroscopic sensors. Take thin-film bulk acoustic resonator (TFBAR) for instance, it operates with a frequency in the range of GHz and offers a high sensitivity to the variations of mass load [22]. Tremendous advances and latest technologies of the sensor structure, manufacturing technology, and signal-processing algorithms have been incorporated into micro and nanosensors and wireless sensor networks [23]. The sensors have now been broadly applied as an integral part in medical diagnostics, chemical, and biological recognition systems, health care, automobile and industrial manufacturing, and environmental monitoring. Among the various sensing materials, ZnO thin films and nanostructures have been widely used for designing and developing of the sensors due to their high sensitivity to the physical, chemical, and biological environment [21].

This chapter will provide an overview of ZnO thin films and nanostructures and their in acoustic wave devices used for microfluidics and sensors applications.

5.2 ZNO THIN FILMS AND NANOSTRUCTURES

ZnO is an “old” semiconductor material, which have been studied for 80 years. The renewed interest is fueled by availability of the new findings on the fundamentals of ZnO and novel applications. ZnO can stably be

crystallized in cubic zinc blende or hexagonal wurtzite structure. The rock-salt structure of ZnO only exists in relatively high pressures. Different crystallized states of ZnO include thin films, nanostructured crystals, and single crystals. However, much attention has been paid for ZnO materials with low dimensions due to the increasing demand of the miniaturized devices, which leads to thorough and extensive investigations on the ZnO thin films and nanostructures. In this section, fundamentals, growth, and deposition techniques of ZnO thin films and nanostructures will be briefly presented; and high-quality ZnO thin films and nanostructures are discussed for acoustic wave devices and sensing applications.

5.2.1 FUNDAMENTALS OF ZNO

The electronic band structure of ZnO is one of the basic properties and has been investigated through the theoretical calculations and experimental determination. The band structure calculation was first proposed using a Greens function method in 1969 [24]. Later, density functional theory method was used. A band gap of 3.77 eV was obtained between the valence band maxima and the conduction band minima at Γ point of the Brillouin zone using a local density approximation (LDA) and atomic self-interaction corrected pseudopotentials [25]. However, simply using the LDA could underestimate the band gap for 0.2 eV [26]. Experimentally, the band gap of the ZnO is 3.37 eV at room temperature and 3.44 eV at low temperatures, which is significantly dependent on the temperature and pressure due to the change of the lattice constants. The Varshni's empirical relation between the band gap and temperature can be written as follows [27]:

$$E_g = E_{g0} - \frac{\alpha T^2}{T + \beta} \quad (5.1)$$

where E_{g0} , α and β correspond to the transition energy at 0 K, a temperature fitting coefficients of -5.5×10^{-4} eV·K⁻¹ and -900 K, respectively. Such a direct and wide band gap of ZnO is beneficial to the optoelectronic applications in the blue and UV regions, including light-emitting diodes, UV laser, and photodetectors that will be discussed later in this chapter. In order to get a larger band gap of ZnO, band-structure engineering has been adopted by doping or alloying with MgO and CdO, which has been considered as an alternative to the wurtzite gallium nitride (GaN)-based optical devices [28,29]. In addition, the high exciton binding energy of 60 MeV ensures

efficient excitonic emission of optoelectronics based on excitonic effects [30], and the laser worked with exciton transition is expected.

Piezoelectric effect is a reversible process that exhibits a linear electro-mechanical interaction between the mechanical and the electrical state in crystalline materials. Piezoelectricity was discovered by French physicists Jacques and Pierre Curie [31]. As an important characteristic of hexagonal wurtzite ZnO, piezoelectricity originates from the polarity that is composed of tetrahedral coordination. The direction of the polarity is along the c -axis from cation to anion, which results in the primary polar plane (0 0 0 1) with the lowest energy. When the external mechanical stress is applied and induces lattice distortion of the wurtzite ZnO materials, the centers of Zn cation and O anion are displaced in the noncentrosymmetric structure and local dipole moments are formed. Accordingly, piezoelectricity along the [0 0 0 1]-direction appears due to the macroscopic polarization in the ZnO crystal. A large electromechanical coupling of k^2 ranging from 1% to 5.2% can be obtained due to the highest piezoelectric tensor of the tetrahedrally bonded ZnO in the II–VI compounds with wurtzite structure [32,33].

In the practical applications, good piezoelectricity requires that the ZnO single crystal or thin film possesses a strong texture, low defects, an accurate stoichiometric ratio of Zn atoms to O atoms, a smooth surface with a low roughness, and an appropriate thickness. Various technologies and methods have been developed to obtain high-quality piezoelectric ZnO materials [34–37]. For instance, in order to increase the piezoelectric constant, different transition-metal atoms (e.g., Fe, V, Cr) doped in ZnO have been reported, and the piezoelectric properties have been significantly improved [34,35]. The piezoelectric properties can also be tailored by tuning the Mg composition in Mg-doped ZnO [36,37]. The size reduction of the ZnO materials to nanoscale can enhance the piezoelectricity. Recent advance on the theoretical computations using the first-principles method has showed that the effective piezoelectric constant of ZnO nanowire is much larger than that of bulk ZnO material due to their free boundary [38]. Giant piezoelectric size effects in the ZnO nanowire were also reported, and the piezoelectric coefficient of 50.4 C m^{-2} can be obtained when the diameter of the nanowires was reduced to 0.6 nm calculated using density functional theory [39].

The optical properties of the ZnO include luminescence and photoconductivity, as well as the refractive index and absorption index. The luminescence of ideal ZnO crystals only refers to the intrinsic near-band-edge emission at the UV region. The free exciton emission can be observed at a low temperature (e.g., 2–10 K) [40]. A number of studies on the free or bound excitons were performed to observe the low-temperature luminescence [41–43].

However, the defects in ZnO materials are inevitable because of the growth conditions during the process of the synthesis and preparation. These result in diverse characteristics of the luminescence at room temperature such as the blue emission, green emission, red emission as well as UV emission. The different forms of the photoluminescences are possibly originated from the oxygen vacancies, zinc interstitials, zinc vacancies, or doubly ionized oxygen vacancies, as well as the free excitons and intrinsic transition [41–43]. Taking the blue emission in ZnO for instance, it was assigned to the transitions of electrons from the shallow donor of oxygen vacancy to the valence band and from the conduction band to the acceptor of zinc vacancy [44]. The later transition was argued that it might not exist due to fewer creations of zinc vacancies in the sputtered ZnO thin film [45]. The interstitial-zinc-related defects were also considered to contribute to the blue emission [46]. The luminescence is heavily dependent on the defects that are sensitively varied in the different growth conditions. The intrinsic transition near band-edge for the high-quality ZnO materials can be used to demonstrate the UV lasing under optical pump conditions [47–49]. Experimental and theoretical investigations have provided an insight into the formation mechanism of those different defects, by combining the luminescence spectroscopy with electron paramagnetic resonance measurements and the theoretically accurate computations [9,50]. The formation of the different defects depends on the growth conditions. Therefore, control of the defect formations in the ZnO becomes an important field in engineering and development of ZnO materials.

Photoconductivity and surface conductivity of ZnO thin film and nanostructures are sensitive to the exposure of the surface to the light and absorbed molecules or atoms, respectively. Photoconductivity is a phenomenon in which the electrical conductivity depends on the absorption of the electromagnetic radiation. Photoconductivity of ZnO, which was first observed by Mollow and Miller, is now extensively investigated [51,52]. Different ZnO materials including thin film, nanostructures, and single crystals have been involved in the evaluation of the performance of photoconductivity. The photoresponse of ZnO changes from tens of microseconds to a few minutes because of the different transitions governed by the intrinsic inter-band or excitonic transition, the surface-related oxygen adsorption/desorption process, or the recombination process [53–56]. Normally, the photoresponse induced by the intrinsic inter-band transition is much faster than those dominant by the oxygen adsorption and the recombination. The different mechanisms of the photoconductivity have been proposed such as the hole-capture model and exciton transition in ZnO, as well as the oxygen adsorption/

desorption for ZnO materials with low dimensions [57,58]. Therefore, high-quality ZnO thin films and nanocrystals are the basic requirement for the high-speed photosensor with a fast response.

The surface conductivity of ZnO is changed with the charge accumulation near the surface due to the band bending when the charge transfer occurs after absorbing various gaseous molecules or atoms. The surface conductivity of ZnO significantly depends on the exposure of the gas and prone to be changed. Surface conductivity of ZnO was investigated by annealing and adsorption of atomic hydrogen or of oxygen in an ultrahigh vacuum chamber [59]. A layer of the surface electrons accumulated on the annealed single crystals was confirmed that could exist in vacuum and disappear in ambient air [60]. The surface defects formed by chemical bonding or physical treatment also play important roles on the surface conductivity, which can increase or hinder the charge transfer [61–63]. The appearance of surface states normally reduces the mobility of the carriers and lead to the decrease in surface conductivity [64]. Furthermore, the research on the surface conductivity is helpful to understand the mechanism of ZnO-based sensors discussed in the later sections.

Owing to the main focus of this review on microfluidic and sensing applications, some related properties of ZnO such as nonlinear optics, pyroelectricity, and thermal conductivity are not discussed here, which can be obtained from the other references [65,66].

5.2.2 ZNO THIN FILMS

ZnO thin film is a layered material with thicknesses ranging from a few nanometers (monolayer) to several micrometers. Lots of the studies on ZnO-thin films mainly focus on five topics, including the properties, growth mechanism, methods of the preparation, preparation technologies, and device applications. The crystalline properties, including the texture, orientation, microstructure, morphology, stress, adhesion, substrate, and defects, are intrinsic to piezoelectric and sensing performance. However, the growth conditions significantly influence on the growth dynamics; therefore, in order to acquire high-quality ZnO thin films, the growth parameters are needed to be optimized. This preliminary work is thoroughly performed before the application of ZnO thin films to fabricate high-performance ZnO-based devices [12,33]. The improvements of the deposition techniques, using physical vapor deposition (PVD), chemical vapor deposition (CVD), and wet chemical method, offer a better control of the crystallinity,

piezoelectric, and electrical properties of ZnO thin films. A reproducible, stable, and robust process is expected for the large-scale production of ZnO thin films with a high quality. Therefore, the crystallinity of ZnO thin films and how to grow ZnO thin films using different deposition techniques are presented and discussed in the following sections.

5.2.2.1 CRYSTALLINE CHARACTERISTICS

Texture in ZnO thin films normally refers to the distribution of the crystallographic orientations. It is changed from nontexture in the polycrystalline thin film to perfect texture in single crystals due to the different growth processes. ZnO thin films with a strong texture can be prepared using various growth techniques including the magnetron sputtering, CVD, pulsed laser deposition (PLD), thermal evaporation, atomic layer deposition, molecular beam epitaxy (MBE), and wet chemical method, etc. In a highly textured ZnO thin film, the preferred orientation is commonly along the $[0\ 0\ 0\ 2]$ direction in a hexagonal wurtzite structure, and the cross-sectional microstructure is generally columnar or rod-like as shown in Figure 5.1(a), whereas nontextured polycrystalline ZnO thin films consist of particle-like fine grains in microstructure. Furthermore, the film texture and microstructure determine the hardness, stress, elastic, and piezoelectric properties. Therefore, control and tailoring the crystalline texture of ZnO thin films on demand is of critical importance toward the device-based applications.

Inclined ZnO thin films with a tilted columnar microstructure, as shown in Figure 5.1(b), can be deposited to allow the excitation of a novel mode wave (e.g., shear wave or dual mode waves) in the acoustic devices [67–70]. Common methods of varying the substrate tilt angle or the angle between the substrate and target have been proposed to acquire above ZnO thin films [71–73]. The *c*-axis zig-zag ZnO thin films have been grown in a multilayered structure using SiO₂ buffer layer, which was used to control the generation of the shear waves [74,75]. Shear waves with suppressed longitudinal wave can be excited in such thin films when the inclined angle of the ZnO thin film approaches a special value.

Substrates and interlayer (or buffer layer) are considered as one important factor to prepare high-quality ZnO thin films. Various substrates such as silicon, glass, fused silica, sapphire, diamond, metal, MgO, and flexible polymer have been applied in the deposition of ZnO thin films [76,77]. The substrate can directly determine the lattice mismatch and thermal expansion mismatch, which results in different microstructures, morphologies and

strains in the deposited ZnO thin films. The *c*-axis-oriented ZnO thin films generally grow faster on the special crystallographic surfaces than those on amorphous substrates [77]. In order to improve the film quality, a buffer layer of ZnO has been used as a seed layer to direct the growth orientation [78,79]. Interlayers of silicon carbide (SiC), GaN, diamond, nanocrystalline diamond (NCD) or diamond-like carbon (DLC) on Si substrates has been used to enhance the texture and crystallinity of ZnO thin films [80–83].

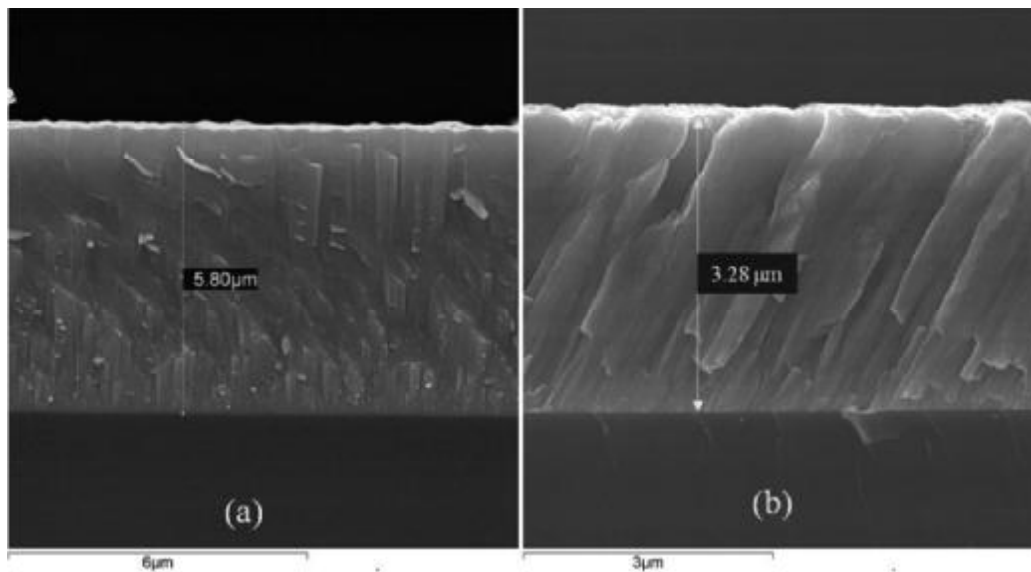


FIGURE 5.1 Textures of the ZnO films on the silicon substrates (a) with columnar structure and (b) with tilted columnar structure measured using scanning electron microscopy (SEM).

Film stress and adhesion to substrate for the ZnO thin films are considered as the key factors to successfully fabricate ZnO-based device in the process of MEMS. The stresses in the ZnO thin films usually originate from the mismatch of the lattice and thermal expansion, which is affected by different growth conditions using various growth techniques. The quantity of the stress can be evaluated using the Stoney formula [84]. Take magnetron sputtering for instance, the compressive stresses often arise through bombardment of the growing film with energetic ions and atoms controlled by the radio-frequency (RF) power, chamber pressure, and deposition rate. Large stress in ZnO thin films could lead to a poor adhesion, resulting in early adhesion failure or delamination. This is one of the major obstacles in manufacturing ZnO-based devices with a high performance. Therefore, reduction in the film stress is critical to improve the adhesion and obtain high-performance ZnO-based devices. Recently, some strategies were adopted, such as

introducing the buffer layer or interlayer, using free-standing substrate or self-standing without substrates, annealing treatment, as well as the optimization of the growth conditions [85,86]. New deposition technique such as high-target utilization sputtering (HiTUS) has also been developed to significantly decrease the stress as shown in Figure 5.2 [84]. Helicon-wave-excited-plasma sputtering was also reported to prepare the ZnO thin film that could exhibit a smooth surface morphology with 0.26-nm-high monolayer atomic steps [87]. In addition, good stoichiometric ratio, low defects, and surface roughness in the ZnO thin films also contribute to crystalline properties. Thereafter, control and improvement of the crystallinity is fundamental. However, it is complicated to enhance the piezoelectric, optical, and electrical properties of ZnO thin films.

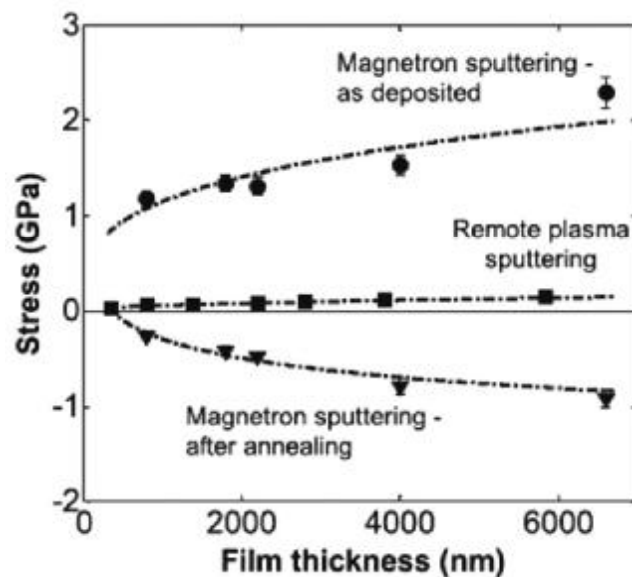


FIGURE 5.2 Comparison of the stresses in ZnO films deposited using the HiTUS technique and normal magnetron sputtering (reprinted with permission from Ref. [84]).

5.2.2.2 GROWTH OF ZNO THIN FILMS

The growths of ZnO thin films have different characteristics due to the various external conditions, which can obviously change the growth dynamics and modulate the crystallizing process. Therefore, the properties of ZnO thin films are various and complicated due to the different growth mechanisms using various techniques such as PVD, CVD, and wetting chemical methods. The balance among the surface free energies of the substrate, film materials, and their interfaces plays a remarkable role on the growth kinetics

that determines the growth mode [88–92]. The interfacial energy is mainly contributed by the strains in ZnO thin films that were mainly formed by the lattice mismatch. When the total free energy of the interface and the film surface is equal to the free energy of the substrate surface, a layer-by-layer (or Frank–van der Merwe) growth occurs [88,89]. For this two-dimensional (2D) growth mode, nucleation of each new layer will only appear after the previous layer is completed. In the opposite case, if the interactions among adatoms are stronger than those of the adatoms within the surface, the three-dimensional (3D) islands or clusters are formed to minimize the interfaces between the thin film and substrate. It is described as the Volmer–Weber growth [90]. However, a common process is an intermediary of the 2D layer and 3D island growth named as Stranski–Krastanov growth [91,92]. A few monolayers usually form first, and subsequently the layer-by-layer growth is transit to islands growth when the thickness of the layer reaches a critical value that is varied with the chemical and physical properties of the substrate and film. Furthermore, the three primary growth mechanism can be transformed due to the variations of the free energies and lattice parameters, which lead to different morphologies and microstructures in ZnO thin films [90]. Appropriate modification of the growth condition could well control the growth mode to prepare the ZnO thin films with special properties. For instance, ZnO quantum dots (QDs) were reported grown on SiO₂/Si substrates using metalorganic CVD (MOCVD) based on the Stranski–Krastanov growth [93]. ZnO QDs were self-assembled by a vapor-phase transport process, and ZnO nanodots with tunable optical properties were achieved on solid substrates in the islands growth mode [94].

PVD technologies are vacuum deposition methods that produce vaporized film materials, following with the condensation at the wafer surface. They consist of sputtering, PLD, thermal evaporation, electron-beam evaporation, and MBE. As a common feature of PVD, ZnO thin-film growth involves a process beginning with the random nucleation and following with stages of nucleation and growth. Nucleation and growth is significantly dependent upon the deposition parameters including the temperature and pressure, growth rate, and substrate surface conditions. This leads to different crystalline phases, orientations, microstructures, film stresses, and associated defects in the ZnO thin films. The unique properties (e.g., size effect) are exhibited from the atomic growth, which cannot be observed in bulk materials.

Sputtering, including direct current sputtering, RF magnetron sputtering and reactive sputtering, is a preferred and popular technique with advantages of simplicity, good reproducibility, low cost, better adhesion, low

operating temperature, and compatibility with microelectronics and MEMS processing. It is a leading choice for the deposition of ZnO thin films in device fabrication. In the sputtering process, the energetic particles bombard on or beneath the surface of the target and generate a lot of atoms or ions that are transported and impinged onto the substrate. The chemical or physical adsorption of atoms or ions leads to the nucleation of. Subsequently, the sputtered atoms collide and diffuse among the ZnO crystal grains, and they grow up and form the ZnO thin film through further condensation and recrystallization. The correlations among the deposition parameters (e.g., chamber pressure, substrate temperature, sputter voltage, bias voltage, and deposition rate), microstructure and the film growth have been discussed thoroughly using a modified Thornton model [95].

Although magnetron sputtering is the most scalable method, plasma bombardment at the surface of the growing film is unavoidable during a typical sputtering deposition. Significant physical changes in the crystallinity could be resulted due to the increase in the plasma density, which leads to more defects and large intrinsic stress in ZnO thin films. High temperature deposition and/or post-deposition annealing can partially improve the film quality; however, they could have problems of incompatibility with the MEMS process. In order to resolve the above problem, a side arm has been developed to generate the plasma that can be launched into the chamber and further steered onto the target using an electromagnet in HiTUS [96,97]. Thus, the low Ar^+ bombardment on the growing film leads to a low ion-induced damage and better control of the roughness and stress for the ZnO thin film (e.g., a roughness of 1.7 nm for 360-nm-thick films) [86].

PLD is a versatile technique that uses the high-power pulse laser beam to ablate and evaporate the surface of the target material. The vaporized materials subsequently form the plasma plume and are impinged onto the substrate to be deposited as a thin film. PLD has advantages of relatively lower substrate temperatures and relative higher oxygen-partial pressure with a wide range than other PVD techniques [98–100]. High-quality ZnO thin films is significantly related to the process parameters of PLD such as the incident laser fluence, oxygen pressure, substrate temperature and substrate to target distance [98,99]. High oxygen background pressure normally results in compressive strain on sapphire and Si substrates, whereas the honeycomb-like morphology is formed at relative low pressure [100]. Thus, the deposition rate and the kinetic energy of ejected species are influenced by oxygen pressure because of the strong collisions between background gas molecules and the ablated species. Owing to the different optimum regimes of oxygen pressure and substrate temperature, a two-step

method was proposed to epitaxially grow ZnO thin films, where the homo-buffer layer was deposited at a low pressure or low temperature, and then subsequently deposited the ZnO thin films at a relatively high pressure or high temperature [101,102]. This method will reduce the surface roughness of the ZnO thin film on glass and sapphire up to 1–2 nm. The substrates (e.g., ScMgAlO_4) with a close lattice match to ZnO can also improve the crystallinity and reduce the defect densities and increase the Hall mobility up to $440 \text{ cm}^2 \cdot \text{V}^{-1} \cdot \text{s}^{-1}$ [103,104]. Recent study showed that the in-plane misfit of epitaxial ZnO thin film on r-plane sapphire were controlled in the range from -1.5% for the $[0\ 0\ 0\ 1]\text{ZnO}/[1\ \bar{1}\ 0\ \bar{1}]$ sapphire to -18.3% for the $[\bar{1}\ 1\ 0\ 0]\text{ZnO}/[\bar{1}\ \bar{1}\ 2\ 0]$ sapphire direction [105]. The strains in the in-plane directions are considered to be generated from the anisotropic lattice matching and thermal contraction of the sapphire substrate. In order to prepare the high-quality ZnO thin films, many buffer layers were also used including platinum, GaN, MgO, SiC, etc. [106–109]. The improvement and optimization of the target–substrate distance and geometry has been done to deposit the ZnO thin films with a large area up to a few inches on sapphire substrate [110]. Novel Aurora PLD method was also developed by applying a magnetic field to the plasma plume, which could significantly reduce the substrate temperature and enhance the photoluminescence [111,112].

MBE is a vacuum atomic layer by atomic layer growth technique invented at the late 1960s [113]. The epitaxial growth is attributed to the crystallographic relation between the film and substrate. The precise control of the reactions of the molecular or atomic beams on the heated crystalline substrate can deposit extremely high purity and highly crystalline thin films. In-situ characterization using reflection high-energy electron diffraction offers real-time growth information to monitor, optimize, and control of the surface structures, lateral uniformity, and growth process [114]. The fraction of nanometer range can be reached for the film thickness using MBE. The evaporated zinc metal and oxygen (or dihydrogen dioxide, H_2O_2) generally are used as the source materials. The growth process of ZnO thin films using MBE is complicated which involves the adsorption, desorption, surface diffusion, incorporation, and decomposition [114]. Furthermore, the growth rate, composition, and doping concentration are mainly dependent on the arrival rates of different species in the collimated beams.

The substrates are crucial to the epitaxial growth of ZnO thin films. The preferred choice is to use the lattice-matched substrates that efficiently reduce the mismatch at the interface, resulting in the decrease in the strain and dislocation between the ZnO film and substrate. The sapphire with a-, c-, or

R-plane, GaN, MgO, and ScAlMgO_4 are most frequently used in the various substrates [115–117]. An epitaxial relationships were found to be $(1\ 1\ \bar{2}\ 0)$ ZnO/ $(0\ 1\ \bar{1}\ 2)$ Al_2O_3 and $[1\ \bar{1}\ 0\ 0]$ ZnO/ $[1\ 1\ \bar{2}\ 0]$ Al_2O_3 with R-plane, and a low density of threading dislocations was observed in the $[1\ \bar{1}\ 0\ 0]$ direction, leading to a high piezoelectric coupling coefficient of 6% [118]. However, the strain is generally large in epitaxial ZnO thin films due to the difference of the thermal expansion coefficients. The buffer layer (e.g., GaN, MgO, ZnS, or SiC) were often used to solve the above problem [119]. An MgO buffer layer has been introduced and promoted the epitaxial growth of ZnO thin films on c-sapphire, resulting in the improvement of the crystallinity and reduction of the screw dislocation density of ZnO layers from $6.1 \times 10^8\ \text{cm}^{-2}$ to $8.1 \times 10^5\ \text{cm}^{-2}$ [120]. Recent advance further showed that the thermal annealed MgO buffer layer can effectively control stress accumulation and produce a high-quality ZnO thin film on sapphire [121].

The MBE growth allows accurate donor or acceptor in the desired thin films. Undoped ZnO is typical n-type semiconductor because acceptors are compensated by native defects. The p-type ZnO thin films can be deposited with good reproducibility using MBE. The acceptor concentration larger than the unintentional donor concentration can be obtained via doping the elements such as N, P, As, and Sb, which is important to develop the ZnO-based light-emitting devices. [122,123]. However, the p-type ZnO thin films are controversial due to their poor reproducibility and instability of electric properties in the acceptor-doped samples. Take ZnO:N for instance, it changed from p-type conductivity to n-type one after a few days and the lattice constants were relaxed to its undoped value [124]. The sputtered ZnO:N thin film with p-type conductivity on glass converted to n-type after repeated measurements in the dark and recovered p-type with exposure to sunlight [125]. The slow transition from p- to n-type conductivity was tentatively assigned to the acceptor migration from the substitutional to the interstitial position [126,127].

In order to deposit ZnO thin films for a large-scale production, CVD technique is developed at the expense of more complicate setup [128–130]. CVD growth is a chemical process that involves the chemical reactions of the gaseous precursors that are delivered into the growth zone using the carrier gas, and the condensation and crystallization of the compounds onto the substrates. Various CVD techniques are categorized according to their operating pressure, such as atmospheric pressure CVD, Low-pressure CVD, and ultrahigh vacuum CVD. Plasma processing was also used to enhance chemical reaction rates of the precursors, leading to the CVD

variants including the microwave plasma-assisted CVD, plasma-enhanced CVD, and remote plasma-enhanced CVD [128]. When the metalorganic species is used as the precursors, this method is known as the MOCVD. It is a preferred and standard technique to grow epitaxial ZnO thin films that exhibits the advantages of good reproducibility, uniform distribution over large area, availability of a wide variety of source materials, excellent control of composition, flexibility of low or high operating pressure, and ability to coat complex shapes [128].

Recently, advances of ZnO thin films have been successfully grown using CVD on different substrates such as glass, sapphire, Si, Ge, GaAs, GaP, InP, GaN, and ZnO [129,130]. The $(1\ 1\ \bar{2}\ 0)$ nonpolar a-plane ZnO films on $(0\ 1\ \bar{1}\ 2)$ r-sapphire substrates can be epitaxially grown, which was expected to fabricate the multimode SAW devices [131]. The pre-reactions in the gas phase using pure oxygen usually cause a significant reduction of the reactor pressure. Thus, alternative oxygen precursors have been proposed including *iso*-propanole, butanole, ozone, ethanol, or N_2O [132,133]. The resolutions for above problem can also be performed by modifying the MOCVD system. The methods such as separating of metal-organics and oxygen flow, controlling of flow patterns and gas residence time, and using horizontal or vertical reactors and high-speed rotation reactors, are efficient to eliminate the prereaction [134,135]. Different metal-organic sources (e.g., zinc acetylacetonate, bis(acetylacetonato) zinc(II), and diethylzinc) are used to produce the high-quality ZnO thin films with better uniformity and reproducibility [136–139].

Although the above growth technologies of ZnO thin films have their advantages and limitations, they are popular and compatible with microelectronics in the device-based application because they could meet the requirements of the MEMS processing. The sol–gel deposited ZnO thin films could not approach the requirements of the fabrication for the SAW devices in spite of the facts that the sol–gel technique is easily operated in low temperature and widely used to prepare the polycrystalline ZnO thin films [140].

5.2.3 ZNO NANOSTRUCTURES

ZnO nanostructures are defined as the ZnO materials consisting of the structural elements with at least one dimension at nanoscale that ranges from 0.1 to 100 nm. The individual ZnO nanostructure refers to the QD, nanoparticle, nanowire, nanorod, nanotube, nanobelt, and nanoplatelet, whereas the

collections of the ZnO nanostructures normally are shown in forms of arrays, assembly, and hierarchical nanoarchitectures based on the above individual ZnO nanostructure. Considering the dimensions at nanoscale, the ZnO nanostructures also are categorized as follows [5,66]:

- zero dimension (0D) nanomaterials, for example, nanoparticle, nano-cluster, nanocolloids, and nanocrystals;
- one-dimension (1D) ones, for example, nanowire, nanorods, nanobelt, and nanotube;
- two-dimension (2D) ones, for example, nanoplatelet and nanodisk; and
- hierarchical three-dimension (3D) nanoarchitectures, for example, nanowire arrays, ordered porous structure, core–shell structure, nanoflower, and brushed shape.

The physical and chemical properties of the ZnO nanostructures are significantly dependent on the size, growth direction, specific shape and microstructure, and this is different with the bulk ZnO materials. Therefore, controllable synthesis of the ZnO nanostructures with multiple functionalities offers the possibility of engineering and developing novel ZnO-based devices.

The unique effects of the ZnO nanostructures include size effect, surface effect, and quantum confinement. They can modulate and tailor the optical, electrical, and piezoelectric properties up to extremely wide regions for specific applications [141]. The size effect is a typical phenomenon linking with quantum effect with the decrease in the size of the ZnO materials to nanoscale, mainly due to the confinement of electrons to very small regions of space in one, two, or three dimensions [141,142]. When the size of the ZnO materials reaches nanoscale the ratio of the surface to volume becomes very large. Thus, the catalytic properties are significantly enhanced, which is usually considered as the surface effect. It is crucial to the sensing applications. The feature of the ZnO nanomaterials in the quantum region is the quantum confinement which was first analyzed by Kubo to interpret the quantum size effect of metals at nanoscale [142]. The continuous energy levels of the electronic structures are split into discrete energy levels. This effect can enhance the optical properties of ZnO nanostructures, for instance, it led to the increase in the band-gap energy of ZnO nanocrystals with the sizes ranging from 3 to 5.4 nm [141].

5.2.3.1 0D ZNO NANOSTRUCTURES

ZnO QDs are typically thought as the 0D ZnO nanostructure. Their discrete energy levels are generated from the excitons confined by the 3D potential well when the dimensions of the ZnO QDs approach or become less than the exciton Bohr radius [142,143]. Many investigations were conducted to understand the excitonic properties of the ZnO QDs, as well as their influences on the optical properties. The exciton Bohr radius for the bulk ZnO is evaluated as 0.9 nm, and the size of the QDs is considered to be 2–3 times larger than the size of the bulk exciton [143]. The electron–hole interaction and quantum confinement effects have comparable strengths for the size ranging from 2 to 6 nm [144]. The quantum confinement of the ZnO QDs leads to the blue shift for the free exciton transition and size dependence of the coupling strength between electron and longitudinal optical phonon in the Raman analysis [145].

Recent advances of the growth of ZnO QDs have mainly been made using the wet chemical methods such as sol–gel technique, solvothermal technique, and hydrothermal technique [146–148]. These methods have changed the environment of the reaction solution including the temperature, the precursor concentration, pH value, and the surfactant forms the external factors that could modulate the size of the ZnO QDs, and subsequently resulting in their tunable optical properties. The obtained ZnO QDs have been used to label the cells with antibacterial activity, low cytotoxicity, and proper labeling efficiency [149]. In order to obtain the emission at special region of the light wavelength, the ZnO QDs were reported to be embedded in graphene, SiO₂ matrix, and PMMA matrix [150–152]. These techniques allowed the applications of the ZnO QDs for the light-emitting devices, for example, the ZnO QDs wrapped in a shell of single-layer graphene could be made a white-light-emitting diode with a brightness of 798 cd·m⁻². The blue-light emitting ZnO QDs combined with biodegradable chitosan (*N*-acetylglucosamine) were used for tumor-targeted drug delivery [153]. Owing to the surface effect, the ZnO QDs were also utilized as sensing materials that exhibited good response to the gas and UV light detections [154,155]. In addition, high-quality self-assemble ZnO QDs can be also grown using the techniques of MOCVD and vapor phase transport [156–158].

The ZnO QDs are special nanoparticles with the size ranging from 1 to 20 nm. When the size is larger than 20 nm and less than 100 nm, the normal ZnO nanoparticles could be stably synthesized using the wet chemical method. The wet chemical method is a low-cost and environmentally friendly technique, which allows control of the shape, size and crystal phase

of ZnO nanoparticles in the solution with mild reaction [159–163]. Since the sol–gel technique is one of the preferred wet chemical growth techniques, the ZnO nanoparticles could be synthesized by the preparation of ZnO sols in the liquid phase from homogeneous ethanolic solutions with precursors of sodium hydroxide and zinc acetate [159,160]. Thus, numerous studies were carried out to explore the growth mechanisms of ZnO nanoparticles with the variations of different solution parameters, which are expected to reproducibly grow ZnO nanoparticles with stable properties for the specific applications such as gas sensing, biosensing, bioimaging and photoelectronic devices [161–163]. For instance, the cytotoxic properties of the biocompatible ZnO nanoparticles against cancerous cells are significantly dependent on the size, and the toxicity becomes greater when the size is reduced. Therefore, an optimum design of the size range could improve the cancer cell electivity and minimize the toxicity against the normal body cells [164].

5.2.3.2 1D AND 2D ZNO NANOSTRUCTURES

1D ZnO nanostructures are the most attractive nanomaterials because of the easy control of the nucleation sites and the diverse device applications. As a typical 1D ZnO nanostructure, ZnO nanowires (or nanorods) has a large aspect ratio of the length to width. The physical properties are remarkable changed with the reduction of the diameter. The Young's modulus and effective piezoelectric constant of the ZnO nanowires are much large than those of the bulk ZnO based on the first-principle computation and experimental measurements [165,166]. However, the structural defects in the ZnO nanowires could delay the response of the electromechanical coupling [167]. In order to grow high-quality ZnO nanowires, various techniques such as vapor phase transportation growth [168] and hydrothermal growth at low temperature [169,170] were developed to control the orientation, diameter, morphology, and position.

Vapor phase transportation growth normally consists of catalyst assisted vapor–liquid–solid (VLS) process and catalyst free vapor–solid (VS) process, which is one of the most popular techniques to synthesize the ZnO nanowires. The metal-catalyzed VLS technique proposed in 1964 is very flexible because the growth parameters are tunable and controllable during the growth process [171]. The typical VLS growth begins with introducing liquid droplets of a catalyst metal with nanosize on the substrate, where the vapor of the ZnO source is condensated, and the nucleated seeds at the liquid–solid interface direct the crystal growth to form ZnO nanowires [172]. The key factor

of growing ZnO nanowires is the size and physical properties of the metal catalyst which determines the size and positions of the ZnO nanowire. The minimization of the total free energy dominates the growth direction which is mainly contributed from the free energy of the interface between ZnO and metal catalyst. When the size of the metal catalysts is reduced, it is a challenging issue to grow ZnO nanowires with such a small diameter because the growth dynamics becomes difficult with the increase in the chemical potential of the liquid alloy droplet. Different metal catalysts (e.g., Au, Ag, Cu, Ni, and Sn) were used to modify the growth directions and morphologies of the ZnO nanowires [172–174]. The ZnO nanowires with a (0 0 0 1) orientation usually can be grown on the a-plane sapphire because of the nearly lattice match epitaxial growth that results in the vertical alignment of the nanowires [175,176]. Some other substrates such as GaN, $\text{Al}_{0.5}\text{Ga}_{0.5}\text{N}$, and AlN also allow the vertically aligned growth of the ZnO nanowire beside the sapphire substrate [177]. Novel crawling growth of ZnO nanowires can be driven on (0 0 0 1) GaN with CVD due to the diffusion of Au from the primary Au-catalyzed particle with large size [178]. Furthermore, the ZnO nanowires can only grow in the activated area with metal catalysts, which allows patterning of the metal catalysts arrays using various lithographical technologies including soft lithography, e-beam lithography, and photolithography [179–181]. Thus, ZnO nanowire arrays with different patterns are controllably grown, which could serve as the highly appropriate device-based materials for the applications of the solar cell, field emission, nanogenerator, and nanolaser [182,183]. The nonlithographical technique using anodic aluminum oxide membranes as a mask can also pattern the Au catalyst on GaN substrate to prepare the ZnO nanowire arrays [184]. It is also noted that the introduction of metal catalysts leads to the impurity level in band gap that could degrade the optical properties, and the metal catalysts may be not compatible with the COMS process in the device fabrication [185]. Naturally considering of the catalyst free VS process, the ZnO thin film on Si substrate was used as a seed layer and the ZnO nanowires were grown using a simple solid–vapor phase thermal sublimation technique [186]. Another method without metal catalysts is MOCVD, which could also obtain the ZnO nanowires on sapphire with high optical quality [187].

Hydrothermal synthesis of the ZnO nanowires at low temperature is a popular growth technique in a solution phase, which has potential for wafer-scale production to fabricate ZnO nanowire-based devices [188]. The ultra-long ZnO nanowires are grown up to several micrometers with the growth time increasing as shown in Figure 5.3(a–d). The aqueous solutions of zinc nitrate and hexamethylenetetramine (HMTA) are often used to prepare the

ZnO nanowires on the ZnO-seeded substrates, with a typical growth process shown in Figure 5.3(e). The high water-soluble HMTA is decomposed to release the hydroxyl ions reacting with Zn^{2+} ions to form ZnO, and the ZnO seeds are nucleated and grown to be the nanowires. The mild reaction conditions are flexibly modified including different substrates, temperatures, reaction times, pH values, surfactants, and substituting zinc acetate and ammonia for the precursors [6,189]. The morphologies of the resulting ZnO nanomaterials with various density and size could be changed from the normal nanowires to patterned nanowires, nanotubes, nanoplate, and flower-like shape [190]. The hydrothermal synthesis of ZnO nanowires can also be assisted by the technologies of applying the electric field, microwave

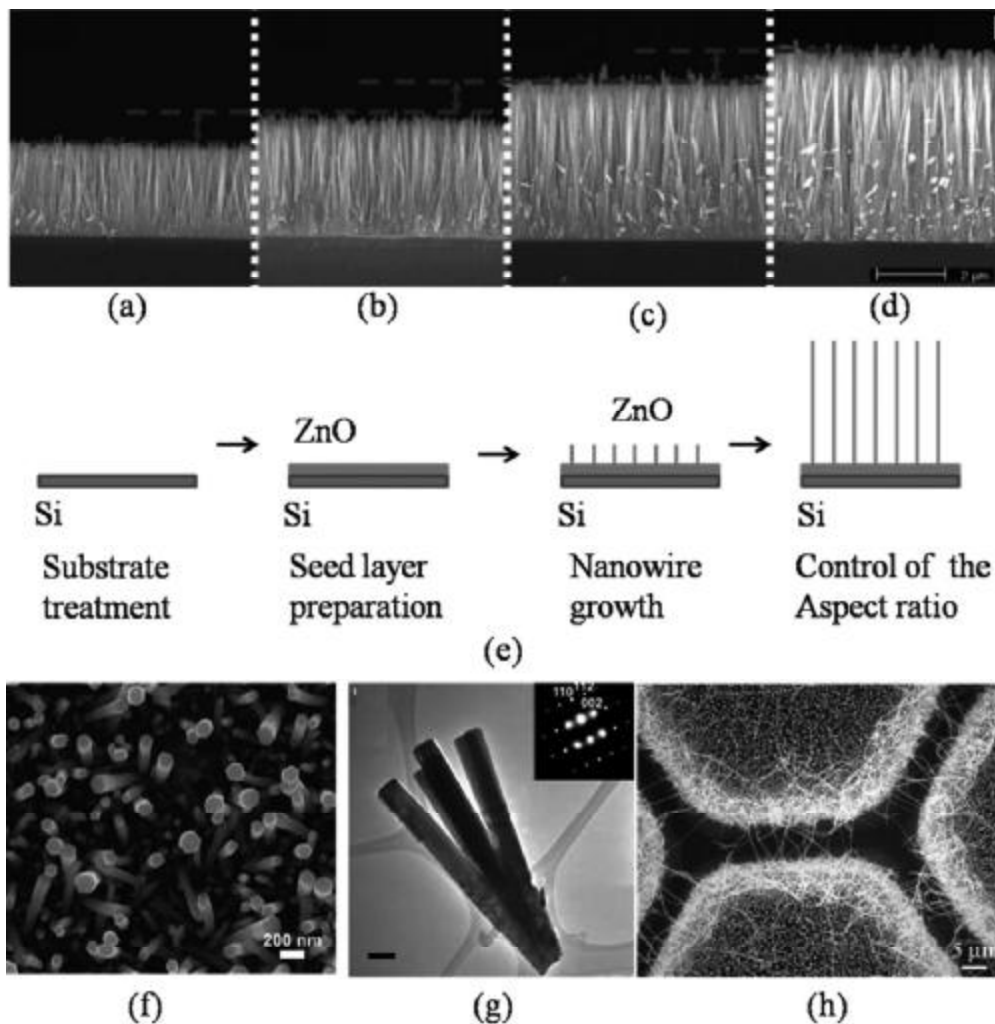


FIGURE 5.3 (a–d) The lengths of the ZnO nanowires increasing with growth times [169]; (e) typical hydrothermal growth process in the aqueous solutions; (f–h) images of SEM and transmission electron microscope for the ZnO nanowires (reprinted with permission from Refs. [168,188,238]).

and laser that allow the rapid growth of long nanowires [191–194]. In addition, the ZnO nanowires can also be prepared using the other wet chemical techniques such as ultrasonic sol–gel technique, spray pyrolysis, and electrochemical deposition assisted by the templates of nanoporous membranes and polystyrene (PS) sphere monolayer [195–198].

ZnO nanobelts normally are long ribbons with a rectangular cross section and well-defined crystallographic surfaces. Wurtzite ZnO possesses two important characteristics: noncentral symmetry and polar surfaces. They dominate the growth of novel structures of ZnO nanobelts by controlling of the growth rates along different directions. The nonpolar facets of $\{2\bar{1}\bar{1}0\}$ and $\{01\bar{1}0\}$ have lower energies than the $\{0001\}$ facets, thus, the ZnO nanobelts dominated by the (0001) polar surface will grow along the *a*-axis [199]. They bend and fold into shapes of nanoring, nanohelices, and nanospring to achieve the minimized energy and neutralize the local polar charges as shown in Figure 5.4(a–c) [4,200]. The polarization of the ZnO nanobelts is perpendicular to the spiral axis for the structures of nanohelices and nanospirals, and a seamless nanoring can be formed with a rotation of 90° for the polarization [201]. The temperature is an important factor to determine the growth direction during the process of the thermal evaporation growth. The ZnO nanobelts began to growing along $[01\bar{1}3]$ before the temperature reach 1475°C and subsequently switched to growing along $[01\bar{1}0]$ with the temperature stabilizing at 1475°C [202]. The effective piezo-coefficient (d_{33}) of the (0001) surface of the ZnO nanobelt measured using piezoresponse force microscopy was found to be frequency-dependent, which is much larger than that of the (0001) surface of the bulk ZnO [203]. Recent investigations showed that the field-emission properties could be enhanced for the ZnO nanobelts [204]. The lasing emission in PL spectra was also found for the ZnO nanobelts, and the sensing application of the ZnO nanobelts for detecting H_2 and NO_2 exhibited fast response and good repeatability [205,206].

ZnO disks and platelets at nanoscale are widely reported as the 2D ZnO nanostructures with example presented in Figure 5.4(d–f). The typical method to synthesize the ZnO disks and platelet at nanoscale is solution phase growth including the microemulsion and hydrothermal growth. When the surfactant of sodium bis(2-ethylhexyl) sulfosuccinate was used during the preparation of an oil-in-water microemulsion, large-scale uniform ZnO disks with diameters of 2–3 μm and thicknesses of 50–200 nm were produced. The morphology of the disk would be modified as hexagonal rings with the increase in temperature from 70 to 90°C as shown in Figure 5.4(d and e)

[207]. If the growth along $[0\ 0\ 0\ 1]$ direction of the wurtzite ZnO is strongly suppressed by the surfactant or capping reagent (e.g., polyacrylamide and ethylenediaminetetraacetic acid), the growth directions along six symmetric directions of $\pm[1\ 0\ \bar{1}\ 0]$, $\pm[1\ \bar{1}\ 0\ 0]$, and $\pm[0\ 1\ \bar{1}\ 0]$ are favored to form the hexagonal ZnO disk during the hydrothermal process. For instance, the ZnO disks and plates can be hydrothermally grown from the aqueous reaction of sodium nitrate and HMTA [208]. Hydrothermal growth of ZnO nanodisks with an average diameter of 150 nm and thickness of 40 nm were reported using ethylenediaminetetraacetic acid as an organic ligand [209]. Double surfactants of hexadecyltrimethylammonium bromide and sodium dodecyl sulfate recently are used to controllably grown the regular hexagonal twinned ZnO nanodisks [210]. The growth along $[0\ 0\ 0\ 1]$ direction of the wurtzite ZnO was recovered without surfactants, then ZnO nanoplates were formed as shown in Figure 5.4(f) [211]. The mixtures of zinc oxide and graphite powders were used as source materials in vapor-phase transport method, resulting in hexagonal nanodisks with about 3 μm in diagonal and 300 nm in thickness [212].

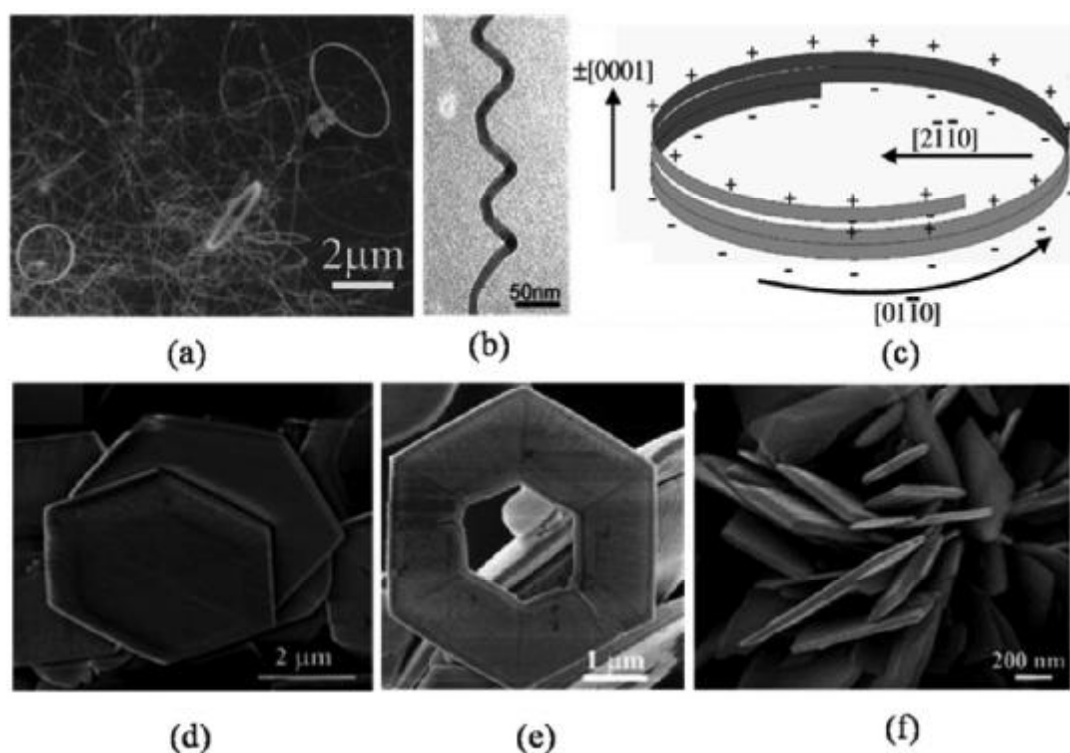


FIGURE 5.4 Different shapes of the ZnO nanobelts: (a) nanoring [4] and (b) nanohelices [200]; (c) the crystallographic orientation of a ZnO nanoring [4]; 2D ZnO nanostructures: (d) hexagonal disk [208], (e) hexagonal ring [208], and (f) platelet [211] (reprinted with permission from Refs. [200,208,211]).

5.2.3.3 HIERARCHICAL ARCHITECTURES OF ZNO NANOSTRUCTURES

Hierarchical architectures of the ZnO nanostructures refer to the 3D structures with multiple levels that are uniformly arranged or constructed in order by the relatively low-dimension nanostructures. Figure 5.5 shows the commonly observed hierarchical ZnO nanostructures, which are categorized as ordered porous nanostructure, core-shell, flower-like shape, and branched nanostructures [213–216]. The unique functionality of the hierarchical ZnO nanostructure can be enhanced from the cooperative coupling of the multiple-level, multiple-dimension, and different compositions. They are stimulating lots of interest on the control of growing various hierarchical architectures, which are expected to be applied for the design and development of highly efficient ZnO-based devices [213–216].

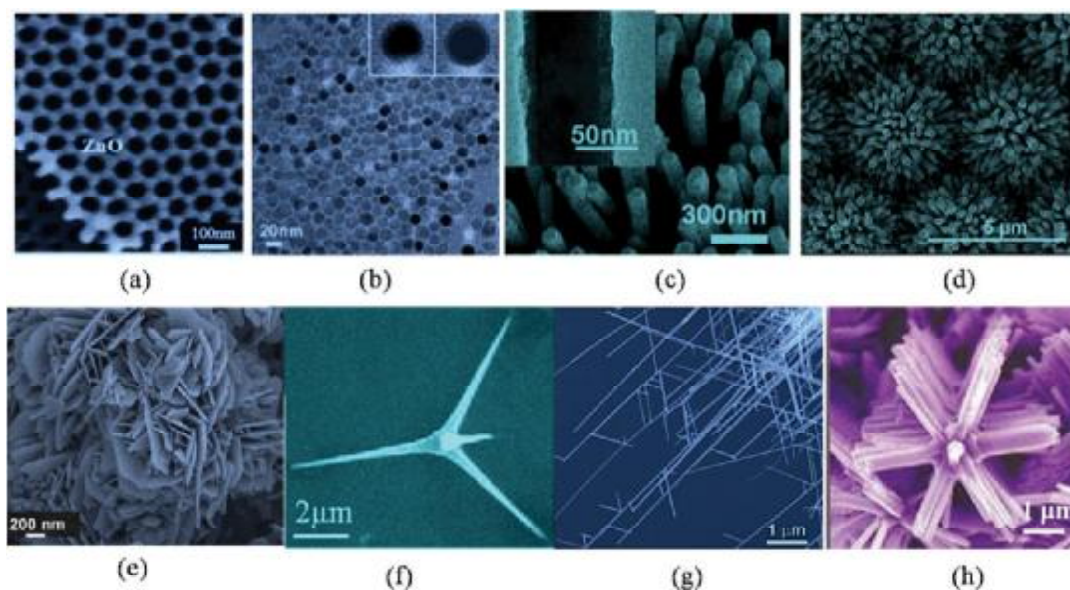


FIGURE 5.5 Hierarchical structured ZnO nanomaterials including (a) ordered porous structure [213], (b and c) core-shell structure [222,223], (d and e) flower-like structure [215,235], (f and h) branched structure [243–245] (reprinted with permission from Refs. [213,215,222,223,235,243–245]).

Ordered porous ZnO nanostructures are normally fabricated using the template method. The templates can be formed using different materials including PS sphere, porous alumina membranes, colloidal crystals, Schiff-base amine, liquid crystals, and ordered mesoporous carbon [213,217,218]. The ZnO materials are filled into the space of the template that is removed later, thus porous ZnO nanostructures are obtained. The pore size, pore

density, and periodicity are determined by the physical parameters of the template, for instance, the smaller PS sphere leads to the rapid reduction of the pore size. Some unique properties of the ordered porous ZnO nanostructures are exhibited, such as superhydrophobicity and high surface area [219,220]. When the PS spheres with a size of 193 nm had been used as the template the products also were considered as inverted 3D photonic crystal structure which helps enhancing the optical property of ordered ZnO nanostructures [221].

Core-shell ZnO-based nanostructures consist of the core-shell nanoparticles and core-shell nanowires, where the ZnO nanocrystals can be grown as either the shell or the core [214,222–225]. Owing to the bandgaps and the relative position of electronic energy levels, two types of the core-shell ZnO-based nanostructures are mainly focused for investigation. The first one is that the band gap of shell nanocrystals is larger than that of the core and the carriers are confined in the core. The second one is that the carriers are partially or completely confined in the shell which is dependent on the thickness of the shell [214]. When the ZnO nanocrystals were selected as the shell materials, they provide energy barriers with the different core nanomaterials such as FePt, Mn:ZnS, Zn, and oxides (e.g., Co_3O_4 , Fe_3O_4 , and TiO_2) at the interface. This allows the properties of the core-shell nanostructures to be tuned via precisely controlling of the size, shape, and composition of the core. For instance, the strong violet PL at 425 nm from the ZnO shell of core-shell Zn/ZnO nanoparticles can be well controlled by adjusting the ZnO shell thickness or annealing during the preparation process using laser ablation in liquid media [224]. FePt/ZnO core/shell nanoparticles exhibited a wide range of semiconducting, magnetic, and piezoelectric properties that were expected to modulate the material's response to magnetic, electrical, optical, and mechanical stimuli [225]. Considering that the nanoparticles with ZnO shell often are applied as QDs system for the bioprobe, the core-shell Mn:ZnS/ZnO QDs have been demonstrated that can be glutathione-functionalized as the time-resolved Förster resonance energy transfer (TR-FRET) bioprobes, which are sensitive to detect a trace amount of biomolecules [226]. When the ZnO nanocrystals were used as the core, selenide (e.g., CdSe), sulfides (e.g., ZnS, Ag_2S , and CuS), and oxides (e.g., ZnMgO and MgO) are widely used as the shell materials [227–229]. Recent advances show that ZnO/CdSe core/shell nanowire arrays can be used as efficient photoanodes for photoelectrochemical water splitting [230], and ZnO/CdSe core/shell nanoneedle arrays significantly help improving the photo-to-current conversion efficiency for solar cell [231]. ZnO/ TiO_2 core-shell nanowires were designed as the electrode film to reduce the recombination

rate in dye-sensitized solar cells. Owing to the relation of the conduction band potentials, the energy barrier hinders the reaction of electrons in core with the oxidized dye in electrode, resulting in the enhancement of the solar-cell performance [232]. Homogeneous core-shell ZnO/ZnMgO nanowires could be grown as quantum well heterostructures, which showed a high optical efficiency at room temperature [233]. Hydrogenated ZnO/amorphous ZnO-doped MnO_2 core-shell nanocables on carbon cloth were reported to be used as supercapacitor electrodes, resulting in excellent electrical performance (e.g., an area capacitance of 138.7 mF cm^{-2} and specific capacitance of 1260.9 F g^{-1}) [234].

Figure 5.5(d and e) presents the typical flower ZnO nanostructures. The nanowire, nanorod, nanoplatelet, and nanodisk often serve as the petal, which self-assembly forms into the flower nanostructures with different morphologies. ZnO flowers were assembled with prism-shaped platelets as shown in Figure 5.5(e), which could be deposited on the FTO-covered glass acting as a photoanode of the dye-sensitized solar cell [215]. The nanowire bundles with a radial shape, snow flake, star-like, and urchin-like morphologies may be thought as the variants of flower-like structures [235,236]. The solution-phase growth with low temperature is traditionally performed as a simple route to get the flower ZnO nanostructures. Hydrothermally synthesized ZnO flower-like nanostructures using the aqueous reaction of zinc nitrite (or chloride) with sodium hydrate (or ammonia) are normally made up of nanowires and nanorods at low temperature with a range of $60\text{--}90^\circ\text{C}$, whereas the temperature increases up to $120\text{--}200^\circ\text{C}$ the flower structure is assembled by nanoplatelets or nanodisks at a relatively high pressure in the Teflon-lined autoclave [237–240]. Although the studies of ZnO flower-like nanostructures are partially driven from the interesting and aesthetic points of view, the functionality of these structures are one of the most attractive factors in the diverse ZnO device-based applications [6–11]. The ZnO nano-flowers with a diameter of 200 nm provide a large surface area and direct channels of electron transport from petals to the stem, which exhibited a good overall conversion efficiency that are higher than that of the films of nanorod arrays with comparable diameters and array densities in solar-cell applications [241,242].

Considering the common feature of the collections of the nanowires, namely, the ZnO nanowires are arranged in order around the core wire; brush-like, tetrapod, dendritic, tree-like, and bunched nanowires are assigned to the branched ZnO nanostructures as shown in Figure 5.5(f–h) [243–245]. The 3D branched ZnO nanostructures possess advantages of large surface area and direct transport pathway for charge carriers, which are applied for the

energy conversion and storage devices [216]. The strategies of growing the branched ZnO nanostructures are usually based on the techniques of sequential catalyst-assisted VLS and solution phase growth. The technique of catalyst-assisted VLS as described in the previous section of ZnO nanowire growth could be adopted to prepare the heterobranched structures. For instance, the hexagonal ZnO nanorods with diameters of about 20–200 nm were reported to grow either perpendicular to or slanted to all the facets of the core In_2O_3 nanowires with diameters of about 50–500 nm; and the vapor phase transport resulted in the typical branched ZnO/ In_2O_3 nanostructures [244]. When the self-catalytic liquid–solid method was combined with the vapor–solid process, ZnO dendritic nanowires were observed in form of 2D web-like structure with homoepitaxial interconnections at the branch-to-arm and branch-to-branch regions [245]. As for the solution phase growth, when the Au catalysts were used to assist the growth of ZnO nanowires, comb-like ZnO nanostructures were produced using the hydrothermal technique [246]. Brush-like ZnO– TiO_2 hierarchical heterojunctions nanofibers were prepared via hydrothermally growing highly dispersed ZnO nanorods on electrospun TiO_2 nanofibers [247]. Nanoforest of hierarchical ZnO nanowires can be observed via modulating the growth rate and controlling of the length-wise growth of the core nanowire and the branched growth during the hydrothermal synthesis [248]. The overall light-conversion efficiency based on the branched ZnO nanowire was almost five times higher than the efficiency using upstanding ZnO nanowires for the dye-sensitized solar cell [248].

The growth methods of the hierarchical ZnO nanostructures are various, and there are many controllable factors during the synthesis process. The hierarchical nanostructure is sensitively changed due to the variations of the growth conditions, resulting in the different mechanism of the assembly process [213–216]. Furthermore, the relation of the difference of the hierarchical structures to the properties of the ZnO materials still deserves study with in-depth; and good theory of the accurately controllable growth has not been elucidated. All the above issues are crucial for hierarchical ZnO nanostructures in the various applications.

5.3 ENGINEERING AND DEVELOPMENT OF ZNO-BASED DEVICES

Engineering and development of ZnO-based devices is complicated as it involves accurately designing and modeling the desired device with a special configuration, preparing the ZnO materials with high quality, pretreating the ZnO materials, fabricating the device, characterizing the devices, and

optimizing the design and remodeling. Since the discovery of ZnO materials, each segment of the above process has been devoted with lots of efforts of science and technology.

Various novel ideas for designing and developing ZnO-based devices have been proposed based on the fundamental properties of ZnO thin films and nanostructures [6,10,12,21,100]. The ZnO associated devices are categorized as follows:

- traditional microelectronic devices, for example, diode, transistor, and supercapacitors;
- piezoelectric devices, for example, SAW device, TFBAR, thin film ultrasonic transducer, and self-power device (e.g., nanogenerator);
- sensors, for example, gas and chemical sensor, biosensor, UV sensor, humidity sensor, wireless sensor, and strain sensor;
- microfluidic devices, for example, pump, mixer, ejector, and atomizer;
- photoelectric devices, for example, solar cells, photoelectrochemical cells, and UV photodetector; and
- optical devices, for example, optical resonator, UV laser and light-emitting device.

The main goal of the engineering and development is to improve the performance of the ZnO-based device. The reproducibility, stability, sensitivity, and efficiency are critical for assessment of a device. Reduction of the size and manufacturing cost also deserves attention to obtain the highly integrated device. In order to realize these, multiple functionalities have been integrated as one unit in some applications [6–12].

Design of the microfluidic attenuation and manipulation using SAWs is one of the most interesting and attractive project, and the SAW microfluidic devices could be comprehensively applied for biomolecular and cellular manipulation, biosensor, drug delivery, biomaterials synthesis, and point-of-care diagnostics [249]. ZnO thin films possess advantages over bulk materials such as device design flexibility, low cost and convenience of fabrication, and compatibility with other integrated microfluidics and sensing technologies. Thus, ZnO SAW microfluidic devices are expected to be highly integrated, more efficient, and stable. Multifunctionality of ZnO SAW microfluidic devices offers a better choice to improve the performance of the microfluidic devices as well as the enhancement of the microfluidic performance and optimization of the acoustic properties [249]. The standard processing in technological details also ensures more reproducible for ZnO SAW microfluidic devices with the same structures.

When ZnO thin films, nanostructures or the mixture of them are exploited for tracing different minor samples in air, bioliquid, and optical environment, the engineering and development of the ZnO-based sensors would be a complicated issue. When various ZnO-based sensors are designed, the high sensitivity, good selectivity, and strong stability are important factors to be pursued. The fundamental properties of the ZnO materials are needed to be optimized using different technologies including growth techniques, fabrication methods, and analytical techniques.

The following sections focus on the advances of the researches on the applications of ZnO SAW device, ZnO SAW microfluidics, and ZnO SAW sensors.

5.4 ZNO ACOUSTIC WAVE DEVICES

The fundamental parameters such as the insertion loss, phase velocity of the acoustic wave, electromechanical coupling coefficient, and quality factor determine the performance of ZnO acoustic wave devices. In order to obtain high-performance ZnO acoustic wave devices, the following factors are necessary to be considered or improved:

- High-quality piezoelectric materials normally contribute large electromechanical coupling coefficient. The stoichiometric ratio, cut direction, dielectric constant, and effective piezoelectric constant all have played important roles on the coupling coefficient of the bulk materials, whereas the piezoelectricity of ZnO thin films are also dependent on the film crystallinity including orientation, surface roughness, thickness, and substrates.
- Pattern design of the electrodes is crucial to the excitation of the acoustic waves. Good structure of the electrode patterns significantly improves the characteristic of the relation between the resistance and frequency as well as the quality of the acoustic signal. For instance, the number of finger pairs, spatial periodicity, aperture, and distance of the two ports for the interdigital transducers (IDTs) could influence the intensity, frequency, and propagation direction of the acoustic waves.
- As for fabricating the device, the physical properties of the electrode materials and the parameters of the configuration for the electrodes provide a complex impedance of the equivalent circuit. The compatibility of the fabrication with silicon technologies is necessary.

Advanced lithography technique such as e-beam lithography could manufacture the high-frequency acoustic device with frequencies at GHz level.

- A standard probe station could help to get accurate information of the device. The connection of the cables among equipment, bonding using different metal wires and the measurement skills are vital to the characterization of the acoustic wave devices.

Herein, ZnO acoustic wave devices mainly refer to the ZnO SAW device, ZnO TFBAR, and ZnO ultrasonic transducer.

5.4.1 SURFACE ACOUSTIC WAVE DEVICES

The ZnO SAW devices are mainly composed of filters, resonators, delay lines, and convolver. An IDT is two sets of connected metallic fingers that are interspaced between each other. A typical ZnO SAW filter has two ports of IDTs that are patterned on the ZnO substrates. The acoustic waves are excited from the input IDT by the applied electric signals, and subsequently the received acoustic waves at the output port are reconverted into electric signals. The acoustic properties of the device could be measured from the signals between the input port and output port, which allow the evaluation of the performance for the ZnO SAW device. Phase velocity (v) of SAW is related to the wavelength (λ) and resonant frequency (f). It is calculated based on the following equation:

$$v = \lambda f \quad (5.2)$$

where the wavelength, λ , corresponds to the spatial period of the fingers in IDT. The phase velocity is dependent on the thickness of the piezoelectric substrate. If the UV-based nanoimprint lithography is combined with lift-off processes, ultrahigh-frequency ZnO SAW device on silicon substrates could be fabricated that have operated resonance frequency at a range of about 4–23.5 GHz [250].

The electromechanical coupling coefficient (k^2) is used to estimate the efficiency of the energy conversion between the electric signal and the SAW, which is generally calculated using the following equation [251]:

$$k^2 = \frac{\pi}{4N} \left(\frac{G}{B} \right)_{f=f_o} \quad (5.3)$$

where N is the finger pairs, and G and B are the radiation conductance and susceptance at the central frequency, respectively. G and B can be measured from the Smith charts of the reflection coefficients at the central resonant frequency of the SAW signals. The strong electromechanical coupling normally leads to a large coupling coefficient, which is influenced by piezoelectricity of the ZnO thin films and the fabrication processing.

In order to obtain a high-performance ZnO SAW device, some hurdles need to be overcome, including the thickness effect, substrate effect, and the second-order effects including the triple-transit effect, metallization ratio effect, SAW reflections and diffractions, and bulk wave generations, etc.

The acoustic properties of the ZnO SAW device are dependent on the thickness of the ZnO thin films. When the thickness of ZnO thin film increases the acoustic velocity in thin film is varied to be close to the bulk value of about 2700 m s^{-1} [252], whereas when the thickness is rapidly reduced, it leads to a decrease in the phase velocity of the SAW that could approach the Rayleigh velocity of the substrate material. This is caused by the stronger penetration of the SAW into the substrate and more energy localization in the substrate. The acoustic wave mode is also changed with the thickness of the ZnO thin film. The Rayleigh SAW could be observed in the thinner ZnO film; however, higher harmonic modes (e.g., second mode known as Sezawa mode) appear with the increase in the thickness of the ZnO thin film as shown in Figure 5.6.

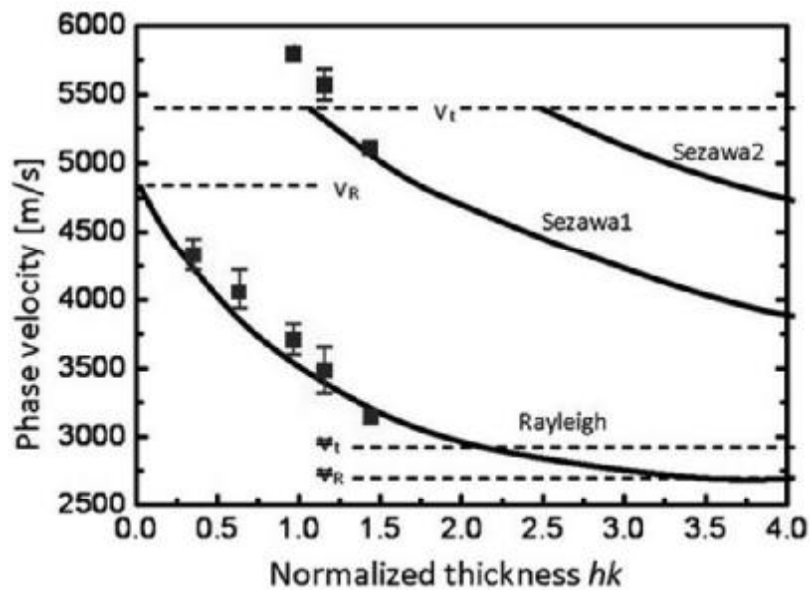


FIGURE 5.6 Phase velocities as a function of normalized thickness (reprinted with permission from Ref. [252]).

Substrate effect means that the difference of the acoustic velocities between the piezoelectric thin film and the substrate affects the acoustic properties of the ZnO SAW devices. The phase velocity in a ZnO thin film is dependent on the acoustic properties of the substrate. The phase velocity of the SAW becomes larger when the ZnO thin film with a fixed thickness is deposited on the substrate with high acoustic velocity such as sapphire, diamond, NCD, or DLC [253–255]. As for diamond materials, including NCD and ultra-nanocrystalline diamond (UNCD), they have the highest SAW propagation velocity, largest elastic modulus, and lowest thermal expansion coefficients. Theoretical simulation and experimental analysis showed that the acoustic energy can be limited within the ZnO and diamond layers, and the propagation loss of the SAW can be significantly reduced using the diamond films [254,256]. For instance, theoretical modeling using the Campbell and Jones method showed that ZnO/diamond SAW device could approach a phase velocity in the range of 7180–10,568 m s⁻¹, k^2 of 1.56–7.01%, and a temperature coefficient of frequency (TCF) of 22–30 ppm °C⁻¹ [257].

Second-order effects often hinder the formation of good acoustic signals. Tripe-transit effect is generated from the interference between acoustic waves that propagate different paths. The useful signals are reflected from the output IDT and sent back to the input IDT, where it is reflected back to the output IDT. The multi-peaks in the form of spurious ripples are often observed for the frequency response of the higher order mode of the SAW. In order to minimize this effect, acoustic absorbers are generally used, and mismatching the finite source and load impedances of the input and output IDTs enable the reduction of this effect at the expense of the increased insertion loss [258]. The effect of metallization ratio is also necessary to be considered in the design and fabrication of the ZnO SAW device. The ratio of the finger width to spatial period has significant contributions to the harmonic signals (e.g., frequency and insertion loss). The thickness of the finger electrodes also affects the central frequency, and variation of the electrode thickness could lead to a distortion of the frequency response. SAW reflections and diffractions are not circumvented due to the acoustic wave properties, thus, appropriately designed structures of the IDTs could minimize this effect.

Recent advances of the ZnO SAW devices have shown that their performances can be enhanced by using high-quality ZnO thin films with multi-layer structures, designing of novel structures of the electrodes (e.g., curved IDTs and circle IDT), and flexible substrates (e.g., polyimide film) [12,259]. Considering the bulk piezoelectric materials which have large coupling

coefficients (e.g., LiTaO_3 and LiNbO_3), ZnO thin films have often been deposited on top of them to fabricate the ZnO-layered SAW devices or called Love mode SAW [260,261]. When Fe-doped ZnO films were used to fabricate high-frequency SAW filters on Si, a better performance was found compared with the SAW filters on undoped ZnO films, for example, the electromechanical coupling coefficient and bandwidth increases up to 75.7% and 14.8%, respectively, while the insertion loss decreases 20.3% [34]. Low-cost deposition of the smooth and continuous ZnO films with densely packed vertical ZnO nanorods on silicon substrates was achieved using a chemical solution method, which was used to successfully fabricate the ZnO SAW device with a well-defined resonant signal [262].

5.4.2 FILM BULK ACOUSTIC RESONATOR

ZnO film bulk acoustic resonators (FBARs) are the devices that consist of a ZnO film sandwiched between two thin electrodes, which were first demonstrated in 1980 [263]. The mechanical resonance is generated from the applied electric field on the input electrode. In order to enhance the resonant signals, the working piezoelectric unit of FBARs is isolated acoustically from the supporting substrates. Three types of the structures can be designed for the back electrodes of FBARs such as Bragg reflector type, air-gap type, and back trench. Considering the ZnO film with a definite acoustic velocity of V , the relation between the thickness (d), and resonant frequency (f_n) is determined as follows [264]:

$$f_n = \frac{\pi(n+1)V}{2d} \quad (5.4)$$

where the natural number, n , corresponds to different resonant modes [261]. This relation clearly shows a thickness effect for FBARs, e.g., the thinner ZnO film results in a higher resonant frequency.

The design of FBARs has less degrees of freedom than that of SAW devices because the frequency is only determined by the layer stack rather than by the lithography technique. The typical electrode materials are gold or aluminum and later Mo was proved to be good success in depositing low-stress electrodes. The performance of FBARs is simply evaluated from the electromechanical coupling coefficient (k^2), quality factor, TCF, area efficiency, and environmental robustness. Here, the area efficiency refers to the utilization of the piezoelectric layer apart from the dead area between resonators in topology and area consumed by interconnects and packaging.

FBARs usually work in the range of a high frequency above 1 GHz, whereas the ZnO SAW devices have low resonant frequency, much lower than 2 GHz. Therefore, FBARs exhibit many advantages of small base mass, high sensitivity, efficient parallel detection by array of FBARs. They can be also integrated with LOC system and microfluidics.

Comparing with those using a longitudinal wave, the damping of the shear wave in a liquid is significantly reduced; therefore, the shear mode in FBARs is a good choice in its applications in liquid. Dual-mode ZnO FBARs with tilted c-axis orientation were investigated, which showed that material properties and bulk wave properties were strongly dependent on the tilt angle. Pure thickness longitudinal modes was found at 0° and 65.4° for the ZnO FBARs, and pure thickness shear modes occur at 43° and 90° [265]. c-Axis inclined ZnO thin films were used in FBAR with Bragg reflector that operated at 850 MHz in the shear vibration mode, with a coupling coefficient of 1.7% and quality factors of 312 in air and 192 in water [266]. Recent study showed that a lateral field excited ZnO FBAR operated in pure-shear mode has a resonant frequency near 1.44 GHz and a Q -factor up to 360 in air and 310 in water, which reached the mass sensitivity of $670 \text{ Hz} \cdot \text{cm}^2 \cdot \text{ng}^{-1}$ and the high mass resolution of $0.06 \text{ ng} \cdot \text{cm}^{-2}$ [267]. Direct comparison of the gravimetric responsivities of ZnO-based FBARs and solidly mounted resonators (SMRs) indicated that the FBARs' mass responsivity was about 20% greater than that of the SMRs' for the specific device design and resonant frequency at about 2 GHz, which was mainly due to the acoustic load at one of the facets of the piezoelectric films in the Bragg reflector [268].

5.4.3 ULTRASONIC TRANSDUCERS

ZnO ultrasonic transducers operated in a large range of 20 kHz–20 MHz are typically applied for nondestructive testing and biomedical imaging [269–271]. Typical ZnO ultrasonic transducers consist of the top electrode, ZnO piezoelectric film, back electrode, and the matching layer on backing materials. The simplest single-element structure is the piston transducer. In the various designs of the ZnO ultrasonic transducers, the piezoelectric properties of ZnO film, acoustic wave modes, electrode size, effects of backing and matching, and array configuration are considered to enhance the performance of ZnO ultrasonic transducers. The resonant frequency (f) in the thickness mode is influenced by the thickness of the ZnO film and their relation is described by the following equation [272]:

$$f = \frac{nV_p}{d} \quad (5.5)$$

where n is an odd integer; the lowest resonant frequency corresponds to $n = 1$; V_p and d corresponds to the acoustic wave velocity and the thickness of the ZnO film. This relation indicates that the resonance only occurs when the thickness is equal to odd multiples of one-half wavelength of the acoustic wave.

Different substrates are widely used to deposit the ZnO films such as metal, silicon, pyrex-glass, and aluminum foil. Thin metal sheets (e.g., stainless steel, aluminum, and carbon steel) are used in the ZnO ultrasonic transducers which are widely used in the commercial ultrasonic transducers [272–275]. The Al foil supported ZnO film was proposed for the underwater ultrasonic transducers in the very high frequency and ultrahigh frequency ranges, and theoretical analysis showed that with spurious-response-free, wide-bandwidth, high-efficiency transducers could be fabricated based on the properly optimizing the thicknesses of the Al foil and the ZnO film [270,271]. The direction of the ultrasonic wave could be focused by depositing the ZnO film on the curved backing substrate as shown in Figure 5.7(a) [272]. The dome-shaped diaphragm has also been fabricated in the ZnO transducer for 200 MHz cellular microstructure imaging [273]. High frequency ZnO transducers with single element have been extensively reported that could be operated in the region of 100–300 MHz for ultrasonic imaging [274,275]. An acoustic lens-based ZnO transducer with a focus distance of 50–80 μm and lens aperture size of 100–400 μm has been fabricated that possesses a very large resonant frequency of 1 GHz as presented in Figure 5.7(b) [275].

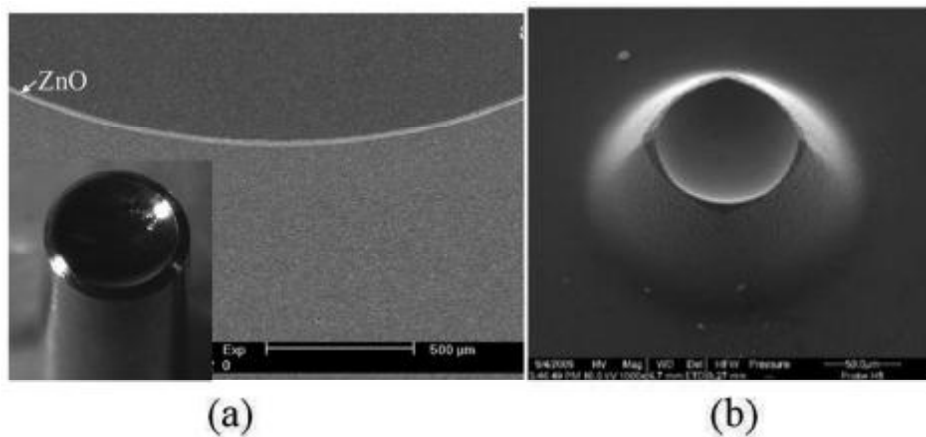


FIGURE 5.7 Deposited ZnO films on the curved backing substrates: (a) sputtering ZnO film on the Al rods [272], (b) the acoustic lens-based ZnO transducer [275] (reprinted with permission from Refs. [272,275]).

However, some issues need to be overcome such as poor resolution out of focal zone and limited frame rate. The scheme of linear arrays is a better way combining the technique of electronically sweeping a beam to solve above problem [276]. The shear mode ZnO ultrasonic transducers were also reported to be operated at a high frequency using the inclined ZnO films [277,278]. The maximum amplitude of the shear mode wave could be accessed when the inclined angle changes at 41° . The c-axis zig-zag ZnO film ultrasonic transducers were also designed for longitudinal and shear wave resonant frequencies and modes using the multilayered c-axis 23° tilted ZnO films [279]. Therefore, high-frequency ZnO ultrasonic transducer array is a promising trend in this field for the biomedical detection and imaging.

5.5 ZNO-BASED ACOUSTIC WAVE MICROFLUIDICS

SAW microfluidics provides a popular and attractive method for LOC system. Various fluidic phenomena can be observed that are applied to enrich the functionality of the microfluidic device. When the SAWs are refracted into the liquid, the acoustic energy is transferred mainly as fluidic kinetic energy in the liquid. The microfluidic actuation and manipulation depends on the coupling of the fluid with SAW, which provides the SAW-based microfluidic devices with advantages of simple, compactness, no moving parts, low-cost, highly biocompatibility, versatility, and easy integration [280].

Comparing with the bulk piezoelectric substrates (e.g., LiNbO_3 , LiTaO_3 , and quartz), ZnO thin films on silicon substrates allow integration of silicon processing technology, microfluidic, and sensing functions into one device, which exhibits advantages of low cost, flexibility, and large-scale production [12,252,254]. This offers new options for the SAW microfluidics using ZnO SAW devices, and tremendous efforts have been devoted to investigate the microfluidic manipulation and control.

5.5.1 THEORY OF SAW-BASED MICROFLUIDICS

The Rayleigh SAW and its harmonics (e.g., Sezawa wave) are often excited on the ZnO SAW devices, which consist of a longitudinal and a vertically polarized shear component. When the Rayleigh SAW encounter a liquid (e.g., a droplet) on the propagation path it refracts into the liquid at a Rayleigh angle that is determined by the Snell law of diffraction, as shown in Figure 5.8 [281]. The Rayleigh angle is calculated using the following formula:

$$\theta_R = \arcsin\left(\frac{c_l}{c_s}\right) \quad (5.6)$$

where c_l and c_s correspond to the velocity of the Rayleigh SAW wave in the liquid and substrate, respectively. For instance, when the Rayleigh wave on a ZnO SAW device is coupled into water liquid, the SAW velocity in water is 1490 m s^{-1} , and that on the ZnO thin film is about 4200 m s^{-1} , and the Rayleigh angle, θ_R , is found to be 20.95° . Of course, the Rayleigh angle will be changed with the wetting property of the divers liquid.

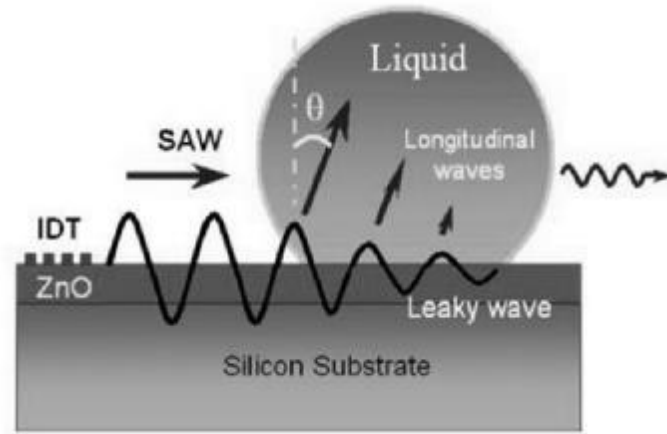


FIGURE 5.8 Schematic illustration of the coupling between the Rayleigh SAW and a liquid droplet (reprinted with permission from Ref. [281]).

When the SAW propagates into the liquid, a net pressure gradient, P , is generated along the direction, which is described as following:

$$P = \rho_0 v_s^2 \left(\frac{\Delta \rho}{\rho_0} \right)^2 \quad (5.7)$$

where ρ_0 and $\Delta \rho$ correspond to the liquid density and the slight density change due to the acoustic pressure. An effective force in the liquid is formed from the net pressure gradient. When the force is not large enough to deform the liquid shape, SAW-induced acoustic streaming occurs in liquid. The streaming pattern is significantly changed with the shape of the confined liquid (e.g., droplet), as well as the incident position, angle, and the operating frequency of the SAW [282]. The induced flow streaming in the liquid droplet is governed by the incompressible 3D Navier–Stokes equations, which are driven by an external acoustic force, F [283]:

$$\frac{\partial U}{\partial t} + (U \cdot \nabla)U = \frac{1}{\rho}F - \nabla P + \eta \nabla^2 U, \quad (5.8)$$

$$\nabla \cdot U = 0 \quad (5.9)$$

where U is the streaming velocity, P is the kinematic pressure, ν is the kinematic viscosity, and F is the acoustic body force due to the presence of the sound source [283]. When the applied RF powers are less than a special value, the droplet can keep in its original shape without inducing significant distortion. Consequently, stress free boundary conditions can be applied at the droplet–air interface. The nonlinear term $(U \cdot \nabla)U$ in Equation (5.9) was ignored, which gives a transient version of linearized hydrodynamic model. Equation (5.9) is simplified as following:

$$0 = \frac{1}{\rho}F - \nabla P + \eta \nabla^2 U. \quad (5.10)$$

Different flow patterns of the SAW induced acoustic streaming in liquid droplet can be simulated combining with the parameters of the SAW and liquid. The careful comparisons of streaming features induced by the SAWs from ZnO and LiNbO₃ SAW devices are expected, which is thought to thoroughly expand SAW induced microfluidics to a more integrated platform for ZnO SAW microfluidic device.

When the applied RF powers are large enough to deform the shape of the liquid, the acoustic force confined in the droplet can be calculated from the asymmetry in these contact angles and the droplet size using the following formula [281]:

$$F_s = 2R\gamma_{LG} \sin\left(\frac{\theta_t + \theta_l}{2}\right)(\cos\theta_t - \cos\theta_l) \quad (5.11)$$

where R is the radius of the droplet and γ_{LG} is the liquid–gas surface energy; θ_t and θ_l correspond to the trailing edge and the leading edge of the droplet on the substrate [281]. This force can generate pumping, ejection, and atomization at extremely large driven powers. These SAW-induced microfluidic phenomena are very complicated due to various boundary conditions, which results in only a few simulations on their nonlinear fluidic dynamics. Although many experimental investigations of the ZnO SAW microfluidics have been reported, the accurately theoretical analysis is still urgently needed to quantitatively reveal the influencing factors in the SAW induced microfluidics.

5.5.2 ZNO-BASED MICROFLUIDIC MANIPULATION AND CONTROL

Using the Rayleigh SAWs excited from the ZnO SAW devices, various studies have demonstrated that the ZnO-based SAW could successfully manipulate the microfluid and particles in liquid and control the fluidic behaviors. Liquid droplets are the main targets that are mixed, pumped, ejected, and heated in the ZnO SAW microfluidics. This offers great potential for the increased throughput and scalability of the microfluidics systems. For instance, the droplet can be used as microreactors, which can be individually streamed, mixed, pumped, ejected, and atomized.

5.5.2.1 MICROSTREAMING AND PARTICLE CONCENTRATION

The microstreaming induced by the SAWs is dependent on the coupling intensity of the SAWs with the liquid. The signal power, droplet position, aperture of the IDTs, and surface roughness could remarkably change the flow patterns in a droplet. When the droplet is placed on the propagation path of the SAW, a butterfly flow pattern with a double vortex pattern is resulted due to the symmetrical distribution of the acoustic energy in the droplet. The quadrupolar streaming patterns could be obtained when the single IDT is immersed in liquid and the bidirectional SAWs are excited.

The streaming velocity in the droplet was found to be linearly changed with the applied voltage of the RF signal, which ranges from 0.2 cm s⁻¹ to 1 cm s⁻¹ as shown in Figure 5.9(a) [281]. The Sezawa wave may be more efficient than the Rayleigh wave for the acoustic streaming. A smaller size of the droplet could obtain a larger velocity when the applied voltage was constant. This has been interpreted from the force–voltage relation that is expressed as the following equation [281]

$$F_s = \alpha(V - V_{th})^2 \left(\frac{\sin[\beta(V - V_{th})]}{\beta(V - V_{th})} \right)^2 \quad (5.12)$$

where α is a force–voltage coupling coefficient and β corresponds to the constant of proportionality relating the input voltage to the temperature-induced frequency shift [281]. The power fed into the acoustic wave has two effects including (1) increasing the amplitude of the acoustic wave and the force acting on the droplet; and (2) a shift in the resonant frequency due to heating. When a flexible ZnO/polyimide SAW device was used in

the acoustic induced streaming, Figure 5.9(b) indicates that a better efficiency of streaming could be reached with a speed of 3.4 cm s^{-1} at a signal voltage of 9.5 V for a 10- μL droplet, as well as the linear relation between the streaming velocity and applied voltage [259].

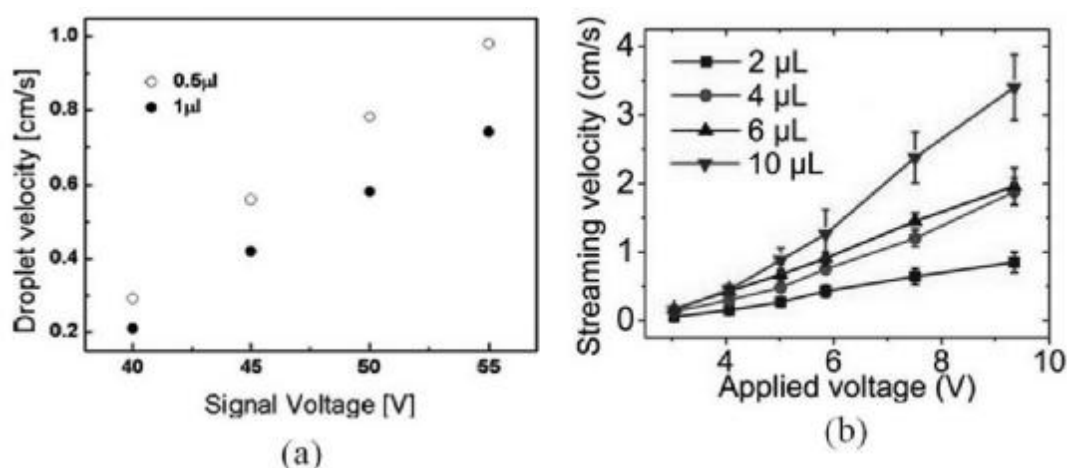


FIGURE 5.9 The relation between the applied voltage and streaming velocity based on the ZnO film (a) on silicon substrate [281] and (b) on the flexible polyimide substrate [259] (reprinted with permission from Refs. [281,259]).

An asymmetric distribution of SAW radiation in the droplet results in the concentration of particles when a droplet with half contact area is placed on the propagation path. Figure 5.10(a) shows the concentration of the particles in droplet using a ZnO SAW device with resonance frequency of 61.2 MHz. This phenomenon can be explained using the similar mechanism proposed from the particle concentration on LiNbO_3 SAW device as shown

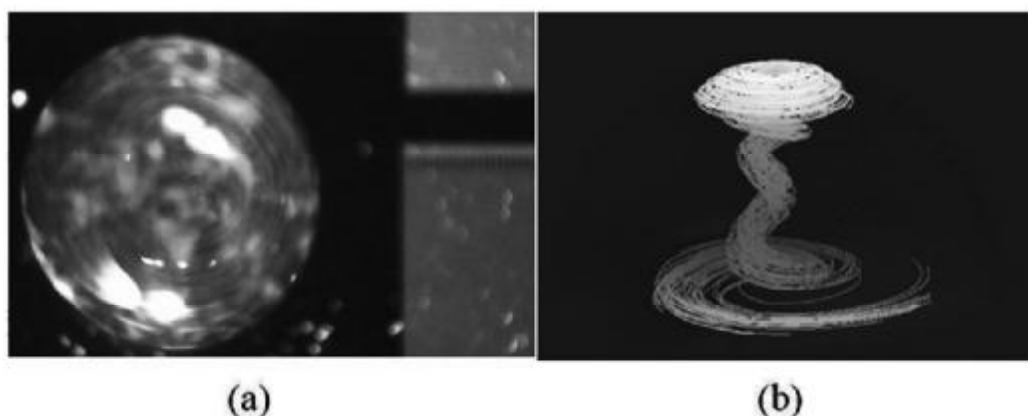


FIGURE 5.10 (a) Concentration of the particles in droplet using a ZnO SAW device and (b) a mechanism of the particle concentration (reprinted with permission from Ref. [283]).

in Figure 5.10(b) [283]. The surface friction hinders the streaming velocity at the bottom of the droplet to be reduced to zero. Thus, a secondary bulk circulation flow is generated from the primary azimuthal rotation flow around the droplet periphery, which produces the swirl-like flow at the bottom of the droplet [14]. The fluid close to the bottom of the droplet moves toward the center stagnation point and takes the particles along with it; thus, the particles can be concentrated near the stagnation area.

5.5.2.2 MICROPUMPING AND LIQUID JETTING

When the RF signal with a high power is applied on the ZnO SAW device, an acoustic force in the droplet is large enough to move the droplet as a micropump. Significant liquid jetting from the original droplet has also been realized at relatively high powers. The surface wetting property of the ZnO film is hydrophilic, that is, the droplet could be stretched along the direction of the SAW propagation. Therefore, the surface treatments are often performed using the hydrophobic polymer layer (e.g., Teflon, CYTOP, or silanization).

The effects of the droplet volume on the pumping velocity of the droplet are shown in Figure 5.11 using a ZnO/Si SAW device [281]. The pumping velocity increases exponentially with the input power. Based on the comparison of the pumping velocities on the ZnO/Si SAW device with those on the ZnO/UNCD/Si SAW device, the pumping efficiency is enhanced for the same droplet size when the acoustic driving force increases as shown in Figure 5.11(b). The pumping velocities are less than 1 cm s^{-1} as shown in Figure 5.11(a) when the UNCD has not been used. The enhancement of the pumping velocity using UNCD interlayer is a combination effect from (1) the increase in the coupling efficiency between the SAWs and the fluids, and (2) the retention of the SAWs near the surface of the devices. The high-quality ZnO films deposited using the advanced HiTUS technique allow the efficient excitation of the SAW due to the high piezoelectricity. The UNCD interlayer with a very low surface roughness can further reduce the dissipation of the acoustic energy into the Si substrate and reduce penetration depth of the Rayleigh wave into the Si substrate, resulting in a strong Rayleigh mode wave and the reduction of the propagation loss of the wave [254,256]. The electromechanical coefficient is also increased by the UNCD-modified ZnO/Si structure [82,254]. However, a quantitative separation of the two effects is difficult. Therefore, a larger driving force is formed by the increased amplitude of the SAW in the acoustic–liquid interaction.

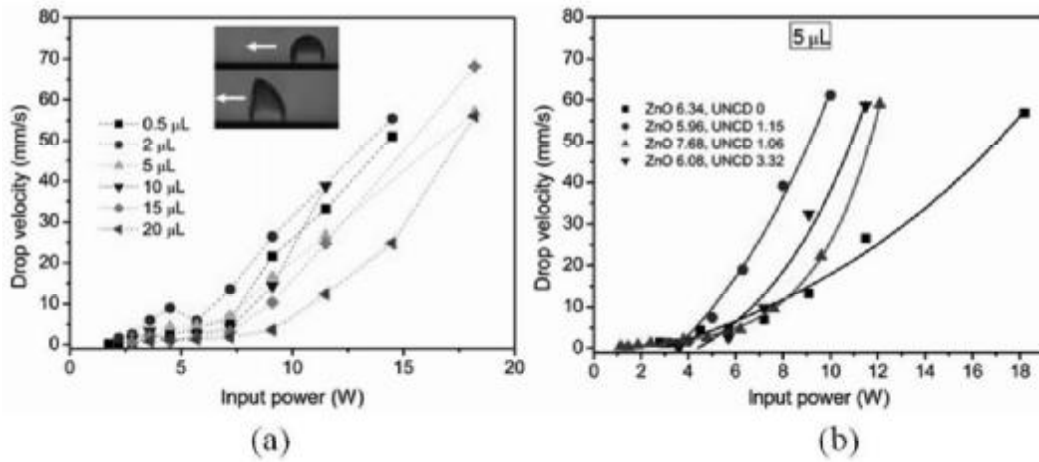


FIGURE 5.11 (a) Pumping velocities of the droplets on ZnO/UNCD SAW devices and as a function of the input power and (b) pumping velocities of the droplets measured from different layered structures (reprinted with permission from Ref. [284]).

An empirical relation between the pumping velocity, V_{pumping} , and input power, P , was found to be the following relation [284]:

$$V_{\text{pumping}} = ae^{P/\beta} + \beta \quad (5.13)$$

where a , b , and β are constants that are mainly dependent on the droplet volume, wetting properties of the surface, the liquid viscosity, and the acoustic property of the ZnO-based SAW devices.

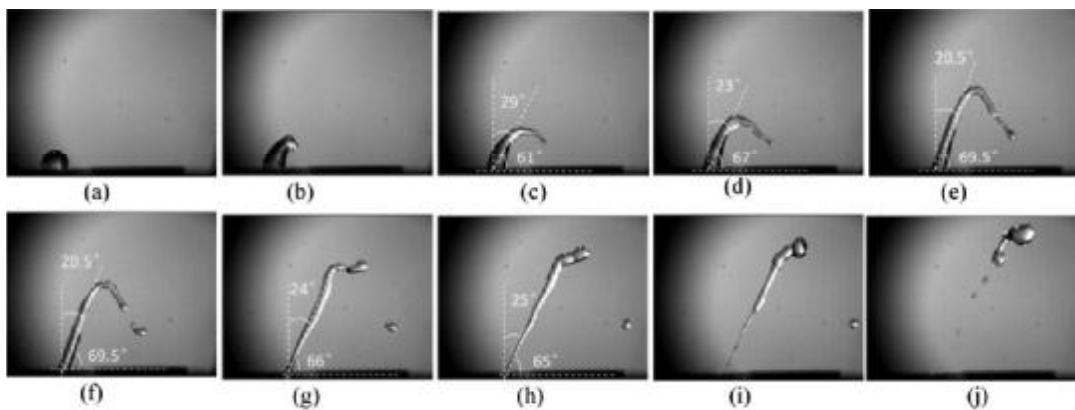


FIGURE 5.12 High-speed images of the liquid ejection for a 5-μL water droplet on the surface of the ZnO/UNCD SAW device (reprinted with permission from Ref. [284]).

If the streaming inside the liquid droplet possesses sufficient inertia to overcome the capillary forces acting on the interface of the fluid and

surrounding media, the drop interface will be deformed, and a liquid jet in the form of an elongated beam was emanated from the free surface of the drop. Early reports of the liquid jetting using the ZnO acoustic wave devices are aiming to the inkjet printing, fuel and oil ejection, and biotechnology [12].

High-speed images provide the detailed process of the liquid ejection for a 5- μL water droplet on the ZnO/UNCD SAW device as shown in Figure 5.12. The maximum jetting angle is also dependent on the droplet volume. Figure 5.13 shows that the shape of the liquid beam changes with the time and droplet size due to the strong propagating loss of the acoustic radiation at the end of the extremely bent liquid beam.

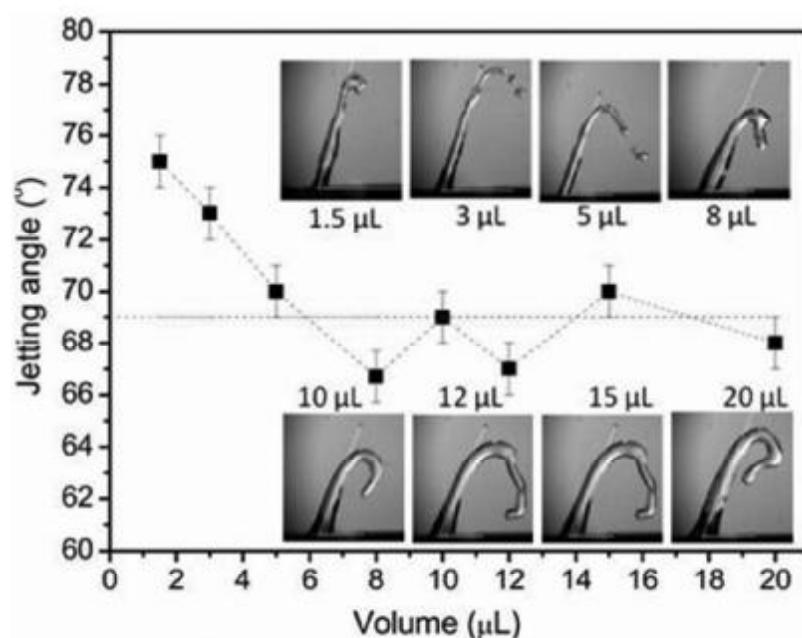


FIGURE 5.13 Maximum jetting angle and beam shape change with the droplet size (reprinted with permission from Ref. [284]).

5.5.2.3 NEBULIZATION AND LIQUID HEATING

Nebulization is the generation of an aerosol of small solid particles or liquid droplets at micron and submicron scale. It is important to a wide range of the numerous applications such as internal combustion engines, drug-delivery device, mass spectrometry, nanoparticle synthesis, agriculture, and cosmetics [280]. The nebulization or atomization has been reported using the ZnO-based SAW device [285]. Some characteristics of the nebulization on the ZnO SAW device are presented here. First, the substrate surface is

hydrophilic and the frequencies of the Rayleigh SAWs are not large (e.g., 11–37 MHz). Second, the nebulization in macroscopic view is like a micro-volcano. Third, the droplet volume is very small (e.g., a few microliter or below) and the ejected satellite tiny droplets are not uniform in size. Figure 5.14 shows the details of the nebulization for a 0.3- μl water droplet. The acoustic pressure induces significant capillary waves on the surface of the liquid droplet that quickly becomes unstable. Some satellite droplets are ejected from the surface following with the generation of a significant mist in the vicinity of the top of the droplet.

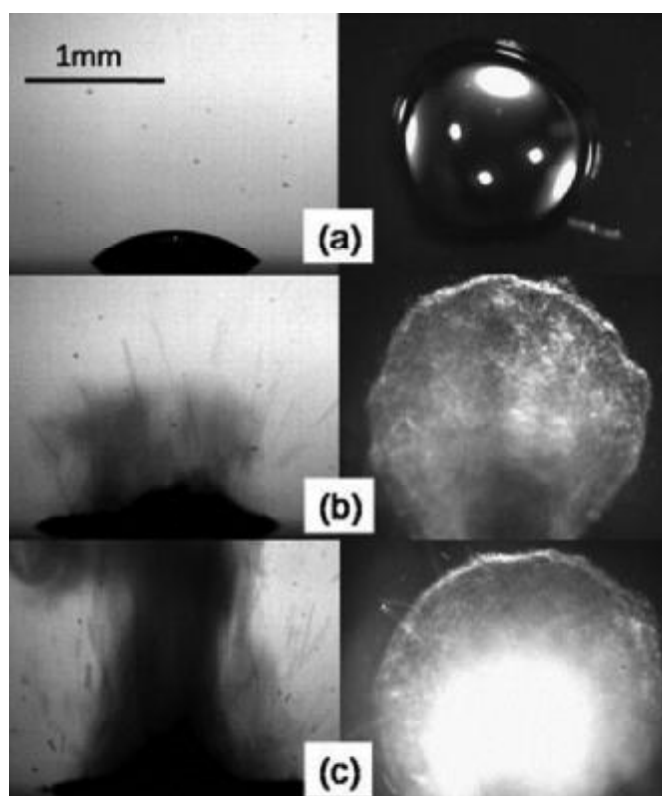


FIGURE 5.14 Typical process of the nebulization on the surface of the ZnO-based SAW device (reprinted with permission from Ref. [285]).

Liquid heating is a thermal effect of the SAWs and widely exists in the SAW induced microfluidics [281]. The increased temperature results in shifts of the resonant frequency of a SAW device, which has an important influence on the accuracy of microfluidic control and the sensing using the SAW devices. The surface temperature of the SAW devices was changed with the applied voltage of the RF signal that is measured using a thermocouple. The temperature range was varied from room temperature to about 120 in 1 min [281]. The thermal image in Figure 5.15(b) clearly shows that

the temperature near the IDT is higher than those in the other area of the SAW device due to the acoustic heating effect from SAW. The temperature variations are proportional to the applied power for the heating rate of the thermal effect in the ZnO SAW device. It is expected to improve the temperature stability by effectively reducing the thermal effect of the ZnO/UNCD SAW device using a diamond layer [284]. The heat could damage the integrity of biological substances and decrease the bioactivity; however, the acoustic thermal effect of the SAW is a good option to assist the polymerase chain reaction (PCR) [286]. Well controlling the increase of the temperature in liquid may be an attractive application in SAW-assisted PCR for the ZnO SAW devices.

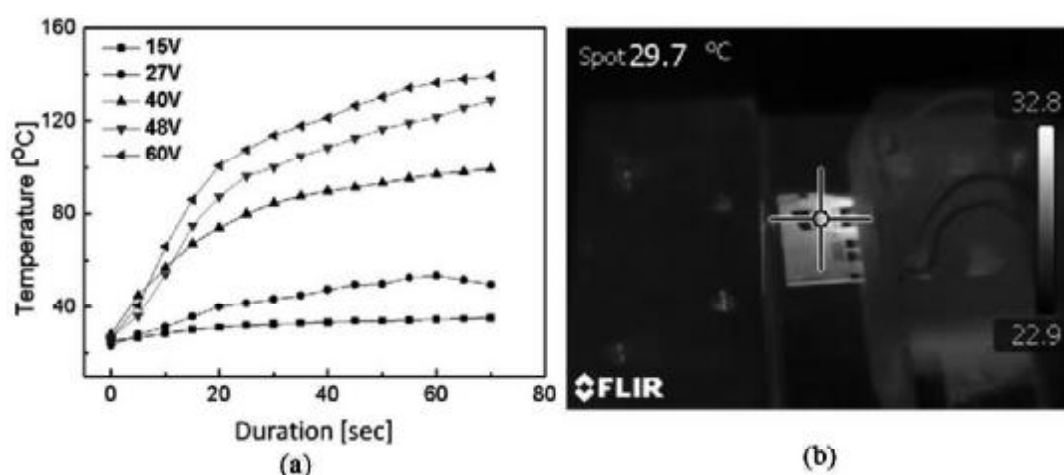


FIGURE 5.15 (a) Thermal effects of the ZnO SAW device and (b) IR images of the ZnO SAW device (reprinted with permission from Ref. [281]).

5.6 ZNO THIN FILMS AND NANOSTRUCTURES FOR SENSING APPLICATION

5.6.1 ZNO SAW SENSORS

ZnO thin films and nanostructures are extensively used for the SAW sensors as well as the other types of the sensors based on the resistance, field-effect transistor, thin-film transistor, and diode. For the principle of the SAW sensors, the SAW will be modulated on the path of the SAW propagation by the sensitive area because the physical properties of the sensing materials are changed by the adsorbed gas molecules, UV light, biological molecules in liquid, or temperature. The responses of the ZnO SAW sensors are resulted in forms of the phase changes, reduction of the insertion loss, or

frequency variations. Furthermore, the perturbations in the velocity of the SAW may be caused from the variations of many parameters including mass load (Δm), conductivity ($\Delta\sigma$), mechanical constant (Δc), dielectric constant ($\Delta\epsilon$), temperature (ΔT), and pressure (ΔP), which is provided as following formula [287]:

$$\frac{\Delta V}{V} = \frac{1}{V} \left(\frac{\partial V}{\partial m} \Delta m + \frac{\partial V}{\partial \sigma} \Delta \sigma + \frac{\partial V}{\partial c} \Delta c + \frac{\partial V}{\partial \epsilon} \Delta \epsilon + \frac{\partial V}{\partial T} \Delta T + \frac{\partial V}{\partial P} \Delta P \right) \quad (5.14)$$

where the dominated factors for the SAW sensors are varied due to the changes in the sensing target. The performance of the sensors could be estimated from the parameters such as the sensitivity, detect limit, selectivity, response time, recovery time, stability, and reproducibility.

In this section, the SAW sensors based on ZnO thin films and nanostructures are focused that mainly involve detecting gases, chemicals, UV lights, and biological molecules.

5.6.1.1 ZNO SAW GAS SENSORS

SAW gas sensors are the techniques that deposit a sensing layer on the SAW devices. The adsorbed gas molecules on the sensing layer could change the acoustic properties of the SAWs on the propagating path and subsequently the variations of the attenuation and velocity of the SAW occur. The perturbation of the SAWs is remarkably dependent on the number of the adsorbed molecules and a large concentration of the gas results in strong modulation of the SAWs [284]. In order to improve the sensitivity, oscillation circuits are designed and a dual-device configuration is often adopted to reduce the interference of the environment (e.g., humidity and temperature). Some other factors also need to be considered in the sensor design and fabrication, such as acoustic vibration mode, substrates, geometry of the IDTs, and the sensing film depositions. Therefore, a good SAW gas sensor can be resulted from the depositing highly sensitive materials, a good compatibility, and integration of the sensor element with the detection system and appropriate analysis methods of the sensing data.

As for ZnO SAW gas sensors, they have two structural types: ZnO sensing layer on the SAW device and the sensing layer with different materials on the ZnO SAW device. For the first type, the ZnO sensing layer with nanostructures is deposited on the surface of the piezoelectric substrates using various growth techniques. The ZnO nanorods were grown on a layered

ZnO/64°-YX LiNbO₃ SAW device using a liquid solution method for H₂ sensing; and sensor response was measured as 274 kHz toward 0.15% of H₂ at 265°C [288]. The electrospun ZnO nanostructured thin film was prepared on a commercial quartz Rayleigh SAW device operated at 433 MHz using an electrospray technique. This sensor exhibited responses to different volatile organic compounds such as acetone, trichloroethylene, chloroform, ethanol, *n*-propanol, and methanol vapor. It is expected to be applied for the sensor array for detecting different volatile organic compounds in a special environment [289].

The different materials are used as the sensing layer on the ZnO SAW device, forming the second-type sensor design. A uniform nanostructured InO_x layer was sputtered on the ZnO/LiNbO₃, which served as a sensor that demonstrated a high sensitivity such as positive frequency shifts of 91 kHz for 2.125 ppm of NO₂ and negative frequency shifts of 319 kHz for 1% of H₂ in synthetic air [260]. Platinum (Pt) and gold (Au) catalyst activated tungsten trioxide (WO₃) selective layers were deposited on a 36° Y-cut LiTaO₃ SAW devices for sensing hydrogen (H₂) concentrations; and frequency shifts of 705 and 118 kHz toward 1% of H₂ in air could be approached, respectively [290]. A 150-nm WO₃ sensing layer was introduced on the 36° YX LiTaO₃-layered SAW device with a 1.2-μm ZnO intermediate layer for sensing ethanol in dry and humid air. It detected 500 ppm of ethanol in synthetic air with frequency shifts of 119, 90, and 86 kHz, corresponding to the relative humidity of 0%, 25%, and 50%, respectively [291]. Palladium (Pt)-coated ZnO nanorods were used as the selective layer that was prepared on the 128°YX-LiNbO₃ SAW device for hydrogen detection. The SAW sensor operated at a frequency of 145 MHz showed a frequency shift of 26 kHz for a hydrogen concentration variation of 6000 ppm at room temperature [292]. A bilayer SAW sensor with a layered structure of WO₃ (about 50 nm) and Pd (about 18 nm) thin films on the Y-cut LiNbO₃ substrate for hydrogen gas-sensing application; the sensing results indicated that the frequency changes correlated very well with decreases of the bilayer structure resistance and the sensitivity was at a level of 2.4 kHz for 4% of hydrogen concentration in dry air [293]. The SAW device with new structures was also reported to be used as a gas sensor, for example, a ball-type SAW sensor was fabricated by sputtering Pt-coated ZnO film as a sensitive film. The sensing measurements showed that the sensor could detect H₂ at a concentration of 20 ppm and the amplitude change of −0.79 dB. When the sensor was wetted by water, it could detect 20 ppm of H₂ with an amplitude change of 0.4 dB, which indicated that the sensitive film was not deteriorated by wetting [294].

In order to improve the sensitivity of the ZnO SAW gas sensors, some assisted techniques are good options, for instance, exploring new sensing materials, designing a sensor array, etc. The selectivity of the ZnO SAW gas sensors are enhanced by adopting appropriate analytical methods including cluster analysis, factorial analysis and regression analysis [295]. Although the ZnO SAW gas sensors have good sensitivity, the selectivity still needs to be improved for the mixture of different gases because the metal or transitional-metal oxides have high affinities to other gases and humidity. If the sensing layer is not active at room temperature, these sensors are normally operated at a high temperature, which limits the wide applications of the ZnO SAW devices in various extreme environments.

5.6.1.2 ZNO SAW UV SENSORS

The SAW UV sensor is to detect the UV light with a wavelength ranging from 400 to 10 nm. The UV-sensitive layer is grown on the SAW propagation path atop of the piezoelectric substrate. When the sensitive layer is exposed for the UV light, electron–hole pairs will be generated and interact with the propagating SAW, thus, the insertion loss of the SAW device increases, and the acoustic velocity will be reduced.

ZnO films serve as a photoconducting layer that can be deposited on the SAW propagating path. A good photoresponse to the slight variation of the acoustic–electric interaction could be detected, which arise from the changes of the sheet resistivity and carrier concentration in the ZnO film [296]. The variations of the velocity and amplitude for the SAW signal can be exploited to monitor the physical variation of the sensing layer, surface, and interface of the multilayers among sensing layers and piezoelectric substrates. They are also influenced by the wavelength and optical power density of the UV light. Typical ZnO-sensing layers have been deposited on the SAW UV sensors. If the thickness of the ZnO film is smaller than the acoustic wavelength, the velocity shift (ΔV) and the attenuation (ΔI) induced by the acoustic–electric interaction could be estimated by the following equations [297]:

$$\frac{\ddot{\Delta V}}{\ddot{\Delta V}_0} = -\frac{k^2}{2} \frac{\sigma_{sh}^2}{\sigma_{sh}^2 + V_0^2 C_s^2} \quad (5.15)$$

$$\ddot{\Delta \Gamma} = \frac{k^2}{2} \frac{V_0^2 C_s \sigma_{sh}}{\sigma_{sh}^2 + V_0^2 C_s^2} \quad (5.16)$$

where V_0 , ΔV , k^2 , C_s , and σ_{sh} corresponds to the SAW velocity on free surface, SAW velocity difference, coupling coefficient, capacitance per unit length of the surface, and the sheet conductivity of the ZnO film, respectively. This indicates that a small downshift of the frequency results in a decrease of the phase velocity, and the amplitude change correspond to SAW attenuation under the UV irradiation. It also indicates that the coupling coefficient k^2 is the key factor to influence the change of velocity and attenuation. A higher k^2 is desirable for a larger acoustoelectric effect and hence a higher sensitivity.

For ZnO SAW UV sensing, the Rayleigh-mode SAW devices can be used to detect the acoustic–electric interaction, and the sensing mechanism have been interpreted [298,299]. For instance, a 200-nm-thick ZnO film was sputter-deposited onto a LiNbO₃ SAW device operated at 37 MHz, which exhibited a large frequency shift of 170 kHz when illuminated using 365-nm UV light with an intensity of 10 mW·cm⁻² [300]. When the 71-nm-thick ZnO thin film was deposited on a LiNbO₃ SAW filter with an operating frequency of 36.3 MHz, its sensitivity could reach a low-level intensity of 450 nW·cm⁻² for the 365-nm UV light [301]. A polycrystalline (poly)3C–SiC buffer layer had been introduced in ZnO/Si structures, which could enhance the sensitivity of the UV SAW sensors from 25 Hz·(mW·cm⁻²)⁻¹ to 85 Hz·(mW·cm⁻²)⁻¹ [302]. Furthermore, nanocrystalline ZnO films with various morphologies of nanoparticles, nanorods, and nanowires have been grown on the Rayleigh mode SAW devices to enhance their photoconductivity [303–306]. Besides the fundamental Rayleigh mode, the Sezawa mode and third-mode harmonics has also been adopted to detect the low-intensity UV light [297,304]. A Mg:ZnO layer was introduced to isolate the semiconducting ZnO layer from the piezoelectric ZnO layer in the ZnO/Mg:ZnO/ZnO/Si structure for the ZnO SAW filter, which exhibited a good sensitivity to a power density of 810 μW·cm⁻² when operated using the Sezawa mode SAW of 711.3 MHz [297]. A large frequency shift of 1.017 MHz could be observed for the 385-nm UV light at a power density of 551 μW·cm⁻² when the Sezawa mode SAW (with a frequency of 842.8 MHz) was used [298]. The response of the ZnO SAW UV sensors were often measured using a network analyzer. However, the ZnO SAW UV oscillator could be designed using an amplifier oscillator circuit, which significantly enhanced the sensitivity [301].

Love mode SAW is a guided wave that is generated from a shear-horizontal acoustic wave propagating in a guiding layer on top of the piezoelectric substrate [261]. SAW device with a Love mode has a good sensitivity to the mass change and photoconductivity variation for applications in liquid biosensing, gas sensing, and photodetection. A 1-μm-thick sputtered

ZnO film on a 90° rotated ST-cut (42°45') quartz SAW device had been reported that did not generate any apparent response texposed using a 365 nm UV light; however, ZnO nanorods grown on the ZnO/90° rotated ST cut (42°45') quartz SAW device significantly increased the UV sensitivity [307]. Therefore, the photoconductivity of ZnO films is related to their crystalline structure and defect properties, which can be varied by controlling the film growth conditions. This enables the sensitivity of the Love mode SAW UV sensor to be optimized through sputtering the ZnO film on a shear-horizontal SAW device under appropriate growth conditions. It is known that rotated 90° ST-cut quartz has a low electromechanical coupling coefficient (k^2) of 0.11% and low dielectric constant of 4.5 [308,309]. However, the 36° Y-cut LiTaO₃ possesses a large k^2 of 4.7% and high dielectric constant of 47, which is beneficial to enhance the sensitivity of the Love mode SAW UV sensor. Love mode SAW UV sensor based on the ZnO/36° Y-cut LiTaO₃ structure was operated at ~41.5 MHz; the amplitude response is -6.4 dB and the frequency shift approached ~150 kHz under a 254-nm illumination at the power density of 350 $\mu\text{W}\cdot\text{cm}^{-2}$ [261]. The summarized performances of the ZnO SAW UV sensors are listed in Table 5.1.

5.6.1.3 ZNO SAW BIOSENSORS

SAW biosensors combine the SAW technique with the biological detector. They form the analytical devices for the analyte sensing based on the biochemical reaction, which could show selective and quantitative responses to the trace amounts of biological samples. SAW biosensors normally consist of the biochemical recognition component, SAW device coated with biospecific layer, and electronic component that process and amplify the output signal [310–312]. The biochemical recognition refers to the bioreceptor that is designed from the interactions of the biomolecules with the target analyte, which is crucial to determining the functionality of the SAW biosensor. The SAW biosensor offers label-free detection of biomolecules and analysis of binding reactions. High selectivity of the SAW biosensor is based on the bioreceptor selectively interacting with the specific analyte against the various chemical and biological components [310–312]. Furthermore, the biochemical reactions in the SAW biosensors are categorized as enzymes, antibody/antigen, nucleic acids/DNA, and cellular structures/cells [312–314]. The ZnO SAW biosensor is utilized based on the advantages of the ZnO piezoelectric films. The ZnO film deposited on the SAW device allows the SAW propagating in this guiding layer and forms the Love mode

TABLE 5.1 Parameters and Sensitivity of the ZnO SAW UV Sensors

Layered Structure	Resonance Mode	Operating Frequency (MHz)	Optical Power Density ($\mu\text{W cm}^{-2}$)	Frequency Shift (kHz)	References
ZnO/LiNbO ₃	Rayleigh wave	37	10	170	[300]
ZnO/LiNbO ₃	Rayleigh wave	36.3	0.45	28	[301]
ZnO/LiNbO ₃	Rayleigh wave	145	500	40	[305]
ZnO particles/LiNbO ₃	Rayleigh wave	64	691	–	[306]
ZnO/Quartz	Rayleigh wave		19,000	45	[303]
ZnO/3C-SiC/Si	Rayleigh wave	122.25	600	150	[302]
ZnO/Mg:ZnO/ZnO/t-Al ₂ O ₃	Sezawa wave	711.3	810	1360	[297]
ZnO/Si	Sezawa wave	842.8	551	1017	[298]
ZnO/Si	Third mode		3000	400	[304]
ZnO nanorods/quartz	Love wave	117	–	–	[308]
ZnO/LiTaO ₃	Love wave	41.5	350	150	[261]

SAW device, which could reduce the acoustic loss into the liquid due to the confinement of the shear-horizontal wave in the guiding layer. Thus, the Love mode SAW is sensitively modulated by the changes of the sensor surface on the propagation path. The guiding layers are deposited using different materials, such as ZnO, polymer (e.g., polydimethylsiloxane and polymethylmethacrylate), SiO₂, and Au [260]. The ZnO and SiO₂ thin films were prepared on the 90° rotated ST-cut quartz SAW devices for immune sensing [314]. The measured mass sensitivity of the Love mode SAW device with ZnO layer was larger than that of with SiO₂ layers, and a high sensitivity of 950 cm² g⁻¹ was detected for the adsorption of rat immunoglobulin G [314]. A highly sensitive Love mode SAW biosensor with a layered structure of ZnO/SiO₂/Si was reported to be designed for the detection of interleukin-6 (IL-6) [315]. Preliminary sensing measurements showed a successful detection of IL-6 protein with a low level when it was operated at 747.7 MHz or 1.586 GHz [315]. The mass sensitivity reached 4.456 μm²/pg when the active areas were functionalized by immobilizing the monoclonal IL-6 antibody onto the ZnO biosensor surface [316]. Mn-doped ZnO multilayer structures were recently used to fabricate Love mode SAW biosensor for detecting blood sugar. The results showed that the reactions of the glucose oxidase with glucose are sensitive with 7.184 MHz mM⁻¹ and stable for about 1 month [317].

Owing to the good integration of the ZnO SAW device with MEMS and COMS processes, novel designs of the ZnO SAW biosensor were recently developed, for instance, COMS-SAW biosensor [318]. A SAW delay line biosensor was fabricated in standard CMOS technology for detecting cancer biomarkers, and the results based on the streptavidin/biotin reaction indicated that the sensitivity reached 8.704 pg Hz⁻¹ and a mass sensitivity of 2810.25 m² kg⁻¹ was detected [318]. Different microfluidic techniques, such as electrowetting on dielectrics, phononic crystal structure, and surface plasmon resonance, were also expected that would be combined with the ZnO SAW biosensors [12,15,286].

5.6.2 ZNO FBAR SENSORS

As a new, effective, and important acoustic sensor technique, the ZnO FBAR sensors could sensitively detect the chemical, biological, and optical variations from the adsorbed species because of their high performance such as the high quality factor and large operating frequency in the GHz regimes. The sensing principle of the ZnO FBAR sensors is similar to the sensor

using the commercial quartz crystal microbalances (QCMs) which operates in thickness shear mode [319]. The resonant frequency of the ZnO FBAR sensors is highly sensitive to the changes of mass, UV light, and biochemical reaction in the working area. This results that the ZnO FBAR sensors are superior to the QCM sensors due to the relatively low resonant frequencies (i.e., less than 100 MHz) for the latter, which provides the advantages with the ZnO and FBAR sensors such as high sensitivity, low hysteresis, label free, good selectivity, and excellent compatibility with the integrated circuit [320]. Therefore, the ZnO FBAR sensors have been widely applied for the mass sensor, biosensor, gas sensor, and UV sensor.

Owing to the high mass sensitivity, the ZnO FBAR sensor with a high operated frequency will be an alternative to the traditional QCM sensors. Typical mass sensing using the ZnO FBAR sensors is that mass loading materials are deposited layer by layer on the top electrode, and the sensitivity is calculated based on the frequency shift, the film area, and film mass. Early work showed that the SMR-type FBAR sensors possessed a high sensitivity of $500 \text{ Hz} \cdot \text{cm}^2 \text{ ng}^{-1}$ that was five orders of magnitude higher than that of $0.057 \text{ Hz} \cdot \text{cm}^2 \text{ ng}^{-1}$ for the commercial 5 MHz QCM [321]. Combining with the CMOS technique, the ZnO FBAR oscillator array with a resonant frequency of 905 MHz could be fabricated for mass sensing, which exhibited a mass sensitivity of $328 \text{ Hz} \cdot \text{cm}^2 \text{ ng}^{-1}$ [322]. A ZnO FBAR sensor with a resonant frequency of 2.44 GHz was measured using a network analyzer and a probe station, which could achieve an excellent sensitivity of $3654 \text{ Hz} \cdot \text{cm}^2 \text{ ng}^{-1}$ for detecting the mass loading layers of titanium [319]. The further comparison of FBAR and QCM-D sensitivity showed that the larger resonant frequency of the ZnO FBAR could increase the sensitivity to the variations in the viscoelasticity of the adsorbent [323]. Based on the mass-loading effect, the ZnO FBAR sensor operated at 830 MHz in shear mode could detect the viscosity of the glycerol solutions up to $10 \text{ mPa} \cdot \text{s}$ [324]. The ZnO FBARs with dual longitudinal modes were designed and fabricated to parallel monitor the mass and temperature changes [325].

Based on the low damping of the bulk wave in liquid, biosensing is one of the important applications for the ZnO FBAR sensors. The backside of the silicon wafer was also etched using deep reactive ion etch to release the free-standing membrane. In the typical biosensing process, the antibodies were adsorbed or coated on the top electrode or the back membrane; the analytes were detected in the liquid through a specific reaction with the antibody on the working area. In order to keep the Q -factor from significantly damping, the channel or cavity structures are generally used to direct or

confine the liquid flowing over the functionalized surface of the ZnO FBAR sensor [325].

There are three trends of the ZnO FBAR biosensors that are rapidly developed including the improvement of the sensitivity, enhancement of the integration with other functions, and expansions of the fields of the biological detections. For instance, when a 750-nm-thick ZnO thin film was sandwiched between the Au and Pt electrodes with a Bragg reflector, a high resonant frequency of 3.94 GHz was obtained [22]. It was used to detect the bio-immobilization mass and the mass of coupling protein up to 380 and 630 pg, respectively, which corresponds to a sensitivity of $8970 \text{ Hz} \cdot \text{cm}^2 \text{ ng}^{-1}$ [22]. Recent sensing investigation of adsorption and antigen binding behavior of monoclonal antibody showed that the ZnO FBAR biosensor operated at about 1.5 GHz could reach $2 \text{ kHz cm}^{-2} \text{ ng}^{-1}$ during the detection of the human prostate-specific antigen [326]. Furthermore, the sensitivity could be enhanced through increasing the sensing area using the nanomaterials (e.g., nanotips or nanowires) and selecting the shear mode bulk wave. A film of the functionalized ZnO nanotips on FBAR using the magnesium zinc oxide ($\text{Mg}_x\text{Zn}_{1-x}\text{O}$) as piezoelectric material were reported to increase the mass sensitivity higher than $103 \text{ Hz} \cdot \text{cm}^2 \text{ ng}^{-1}$ for selectively immobilizing DNA [327]. Beside the longitudinal mode, the shear mode was used for the FBAR biosensor with a inclined angle of 16° in the ZnO piezoelectric film to measure the model system avidin/anti-avidin, resulting in a sensitivity up to $585 \text{ Hz} \cdot \text{cm}^2 \text{ ng}^{-1}$ [328].

Considering the flexible design of the microfluidic structure, the ZnO FBAR biosensor array was placed and sealed in a flow cell consisting of an acrylic glass chamber with an inflow and outflow that were connected to a fluidic system [328]. A microfluidic channel was integrated with the ZnO FBAR biosensor to keep the quality factor up to 150 in the liquid environment [326]. The competitive adsorption and exchange behavior of proteins were monitored among the proteins of albumin (Alb), immunoglobulin (IgG), and fibrinogen (Fib); and a minimum detectable mass was reached for 1.35 ng cm^{-2} [329].

The ZnO FBAR biosensors are also used to detect the enzymatic reactions as well as the model system of the immune reactions (e.g., avidin/anti-avidin, IgE/IgG). The odorant-binding protein were reported to detect the *N,N*-diethyl-metatoluamide using a ZnO FBAR biosensor with a resonant frequency of about 1.5 GHz [326]. The sensing layer was made by immobilizing the acetylcholinesterase enzyme on one of the faces of the shear mode ZnO FBAR resonator with a resonant frequency of 1.47 GHz and Q-factors of 411 in air and 298 in dimethylformamide liquid, which could detect the

organophosphorous pesticides with a very low concentration of 4.1×10^{-11} M [330].

The gases can also be detected using the ZnO FBAR sensors at room temperature combining the sensing materials. For instance, a frequency downshift of 131 kHz was observed with a response time of 12 s under the exposure of 1.4 ppm [331]. The nerve gas could be monitored through coating the poly(vinylidene fluoride) on the top of the ZnO FBAR with a W/SiO₂ Bragg reflector, which showed the gas sensitivity of 718 kHz ppm⁻¹ and a good linear correlation in the range of 10–50 ppm between the frequency shifts and the concentrations of the nerve gas [332]. When a Pd thin film was deposited on the piezoelectric ZnO film as the electrode and sensing layer, the ZnO FBARs with an A/W Bragg reflector and resonant frequency of 2.39 GHz could capture hydrogen to reach a detection limit of 0.05% at room temperature [333].

As described previously about the fundamental properties, the photoconductivity of the ZnO films is prone to changing with the defects. The ZnO FBARs can be applied as the optical sensors to monitor the UV light and infrared (IR) light. The UV sensing with ZnO FBARs were demonstrated that the resonant frequency was increased under the exposure to the UV illumination [334]. The sensitivity could reach 9.8 kHz for the 365-nm UV light with the intensity of 600 $\mu\text{W cm}^{-2}$ [334]. Further studies of the effects of temperature, relative humidity, and reducing gases on the UV response of ZnO-based FBAR showed that the response of the ZnO FBAR UV sensor degraded with the increases in the temperature and relative humidity; reducing the gases (e.g., acetone) also degraded the UV sensitivity [335]. The reason was that the adsorbed oxygen was influenced by the temperature, water molecular, and gas molecular [335]. Thickness field excitation FBAR and lateral field excitation FBAR were reported to detect the IR light, corresponding to the detection limits of 0.7 and 2 $\mu\text{W mm}^{-2}$, respectively. The sensing principle was explained based on the temperature-dependent Young's modulus of the ZnO film, which subsequently resulted in the resonant frequency shifts [334].

5.7 SUMMARY AND FUTURE TRENDS

This chapter presents a comprehensive review of the ZnO thin films and nanostructures for the acoustic wave microfluidic and sensing applications. The fundamental properties of the ZnO thin film and nanostructures are dependent on the growth techniques and growth conditions. The good

piezoelectric ZnO thin films possess large electromechanical coupling coefficient that could be fabricated for the ZnO SAW devices with a better acoustic performance. The SAWs can be excited to mix, stream, pump, eject, and atomize the liquid. Therefore, the ZnO SAW devices are very attractive to be integrated into a LOC system where the SAWs can transport biofluids to the desired area, mix the extracted DNA or proteins, and detect the changes of the signals. The ZnO SAW devices in combination with different sensing layers could be also used to successfully detect the gas, UV light, and biochemicals with remarkable sensitivity.

Although the studies of ZnO thin films and nanostructures have obtained great achievements and large success, the huge space of the research and development for future is still left. The multifunctional integration is promising for the ZnO SAW devices, such as combining with surface plasma resonance, electrowetting dielectrics, and phononic crystal structures. The novel design of the acoustic wave devices are interesting to enhance the microfluidic and sensing applications. They can excite new ideas for the various possible applications based on in-depth understanding the acoustic properties. The coupling mechanism of the acoustic wave with the fluids is sensitive to the deformation of the interface, which is difficult to predict; accurate interpretations of the interaction between the SAW and fluids is urgently needed for the design of novel microfluidic devices.

The ZnO FBAR sensor exhibited an excellent sensitivity for monitor the changes of the mass, bioreactions, gases, UV, and IR lights. The high resonant frequency and Q -factor are vital to the performance of the sensors, which will be improved with the new designs of the structures. The multiple functions are the future trends of the ZnO FBAR sensors highly integrated with different sensing materials and MEMS technique. However, some environmental perturbations still need to be overcome such as the temperature, humidity, optical response and the vibration from the holders. The mechanism of the special sensing processes is also not interpreted well when the physical parameters are monitored. The low cost, portable, high throughput, and miniature ZnO FBAR sensors are pursued with the development of the fabrication techniques in future.

ACKNOWLEDGMENTS

This work is supported by the University's development fund (grant number 201343) and Doctoral research fund (grant number 2014QDJ017) from Xi'an University of Science and Technology, the National Natural Science

Foundation of China (NSFC grant numbers 11504291 and 11504292), UK Engineering Physics and Science Research Council (EPSRC grant number EP/P018998/1), Newton Mobility Grant (grant number IE161019) through Royal Society and NFSC, Royal Society of Edinburgh, Carnegie Trust Funding, the Royal Society-Research Grant (grant number RG090609), and Scottish Sensor System Centre (SSSC).

KEYWORDS

- zinc oxide
- thin film
- nanostructure
- piezoelectric
- microfluidics
- surface acoustic wave
- lab on chip

REFERENCES

1. Hull, R.; Jagadish, C.; Osgood, Jr., R. M.; Parisi, J.; Wang, Z.; Warlimont, H. *Zinc Oxide from Fundamental Properties towards Novel Applications*. Springer-Verlag: Berlin Heidelberg, 2010; p 2.
2. Honerlage, B.; Levy, R.; Grun, J. B.; Klingshirn, C.; Bohnert, K. *Phys. Rep.* **1985**, *124*, 161.
3. Brown, H. E. *Zinc Oxide, Properties and Applications*. Pergamon Press, New York, 1976.
4. Ding, Y.; Kong, X. Y.; Wang, Z. L. *Phys. Rev. B: Condens. Matter* **2004**, *70*, 235408.
5. Fan, Z.; J. Lu, G. *J. Nanosci. Nanotechnol.* **2005**, *5*, 1561.
6. Schmidt-Mende, L.; MacManus-Driscoll, J. L. *Mater. Today* **2007**, *10*, 40.
7. Janotti, A.; Van de Walle, C. G. *Rep. Prog. Phys.* **2009**, *72*, 126501.
8. [8] Wang, Z. L. *J. Phys.: Condens. Matter* **2004**, *16*, R829.
9. McCluskey, M. D.; Jokela, S. J. *J. Appl. Phys.* **2009**, *106*, 071101.
10. Zhang, Q. F.; Dandeneau, C. S.; Zhou, X. Y.; Cao, G. Z. *Adv. Mater.* **2009**, *21*, 4087.
11. Djurišić, A. B.; Ng, A. M. C.; Chen, X. Y. *Prog. Quant. Electron.* **2010**, *34*, 191.
12. Y. Q. Fu, Luo, J. K.; Du, X. Y.; Flewitt, A. J.; Y. Li, Markx, G. H.; Walton, A. J.; Milne, W. I. *Sens. Actuators, B* **2010**, *143*, 606.
13. Abgrall, P.; Gue, A.-M. *J. Micromech. Microeng.* **2007**, *17*, R15.
14. Friend, J.; Yeo, L. Y. *Rev. Mod. Phys.* **2011**, *83*, 647.
15. Haeberle, S.; Zengerle, R. *Lab Chip* **2007**, *7*, 1094.

16. Luo, J. K.; Fu, Y. Q.; Li, Y.; Du, X. Y.; Flewitt, A. J.; Walton, A. J.; Milne, W. I. *J. Micro-mech. Microeng.* **2009**, *19*, 054001.
17. Yeo, L. Y.; Friend, J. R. *Biomicrofluidics* **2009**, *3*, 012002.
18. Wixforth, A. *JALA* **2006**, *11*, 399.
19. Campanella, H. *Acoustic Wave and Electromechanical Resonators: Concept to Key Applications*; Artech House: Boston/London, 2010; pp 38–46.
20. Wise, K. D. *Sens. Actuators, A* **2007**, *136*, 39.
21. Wei, A.; Pan, L.; Huang, W. *Mater. Sci. Eng. B* **2011**, *176*, 1409.
22. Yan, Z.; Zhou, X. Y.; Pang, G. K. H.; Zhang, T.; Liu, W. L.; Cheng, J. G.; Song, Z. T.; Feng, S. L.; Lai, L. H.; Chen, J. Z.; Wang, Y. *Appl. Phys. Lett.* **2007**, *90*, 143503.
23. Voiculescu, I.; Nordin, A. N. *Biosen. Bioelectron.* **2012**, *33*, 1.
24. Rossler, U. *Phys. Rev.* **1969**, *184*, 733.
25. Vogel, D.; Krüger, P.; Pollmann, J. *Phys. Rev. B: Condens. Matter* **1995**, *52*, R14316.
26. Schroer, P.; Kruger, P.; Pollmann, J. *Phys. Rev. B: Condens. Matter* **1993**, *47*, 6971.
27. Varshni, Y. P. *Physica* **1967**, *34*, 149.
28. Ohtomo, A.; Kawasaki, M.; Koida, T.; Masubuchi, K.; Koinuma, H.; Sakurai, Y.; Yoshida, Y.; Yasuda, T.; Segawa, Y. *Appl. Phys. Lett.* **1998**, *72*, 2466.
29. Makino, T.; Segawa, Y.; Kawasaki, M.; Ohtomo, A.; Shiroki, R.; Tamura, K.; Yasuda, T.; Koinuma, H. *Appl. Phys. Lett.* **2001**, *78*, 1237.
30. Bagnall, D. M.; Chen, Y. F.; Zhu, Z.; Yao, T.; Koyama, S.; Shen, M. Y.; Goto, T. *Appl. Phys. Lett.* **1997**, *70*, 2230.
31. Manbachi, A.; Cobbold, R. S. C. *Ultrasound* **2011**, *19*, 187.
32. Corso, A. D.; Posternak, M.; Resta, R.; Balderschi, A. *Phys. Rev. B: Condens. Matter* **1994**, *50*, 10715.
33. Pang, H. F.; Garcia-Gancedo, L.; Fu, Y. Q.; Porro, S.; Gu, Y. W.; Luo, J. K.; Zu, X. T.; Placido, F.; Wilson, J. I. B.; Flewitt, A. J.; Milne, W. I. *Phys. Status Solidi (a)* **2013**, *210*, 1575.
34. Luo, J. T.; Pan, F.; Fan, P.; Zeng, F.; Zhang, D. P.; Zheng, Z. H.; Liang, G. X. *Appl. Phys. Lett.* **2012**, *101*, 172909.
35. Chen, G.; Peng, J. J.; Song, C.; Zeng, F.; Pan, F. *J. Appl. Phys.* **2013**, *113*, 104503.
36. Emanetoglu, N. W.; Muthukumar, S.; Wu, P.; Wittstruck, R.; Chen, Y.; Lu, Y. *IEEE Trans. Ultrason., Ferroelect. Freq. Contr.* **2003**, *50*, 537.
37. Chen, Y.; Emanetoglu, N. W.; Saraf, G.; Wu, P.; Lu, Y. *IEEE Trans. Ultrason., Ferroelect. Freq. Contr.* **2005**, *52*, 1161.
38. Xiang, H. J.; Yang, J.; Hou, J. G.; Zhu, Q. *Appl. Phys. Lett.* **2006**, *89*, 223111.
39. Agrawal, R.; Espinosa, H. D. *Nano Lett.* **2011**, *11*, 786.
40. Park, W. I.; Jun, Y. H.; Jung, S. W.; Yi, G.-C. *Appl. Phys. Lett.* **2003**, *82*, 964.
41. Grabowska, J.; Meaney, A.; Nanda, K. K.; Mosnier, J.-P.; Henry, M. O.; J.-R. Duclère, McGlynn, E. *Phys. Rev. B: Condens. Matter* **2006**, *71*, 115439.
42. Wu, K.; He, H.; Lu, Y.; Huang, J.; Ye, Z. *Nanoscale* **2012**, *4*, 1701.
43. Main, K.; Shimada, R.; Fujita, Y.; Neogi, A. *Phys. Status Solidi (RRL)* **2013**, *7*, 1089.
44. Lin, B.; Fu, Z.; Jia, Y. *Appl. Phys. Lett.* **2001**, *79*, 943.
45. Zhang, D. H.; Xue, Z. Y.; Wang, Q. P. *J. Phys. D: Appl. Phys.* **2002**, *35*, 2837.
46. Zeng, H.; Duan, G.; Li, Y.; Yang, S.; Xu, X.; Cai, W. *Adv. Funct. Mater.* **2010**, *20*, 561.
47. Bagnall, D. M.; Chen, Y. F.; Zhu, Z.; Yao, T.; Koyama, S.; Shen, M. Y.; Goto, T. *Appl. Phys. Lett.* **1997**, *70*, 2230.
48. Tang, Z. K.; Wong, G. K. L.; Yu, P.; Kawasaki, M.; Ohtomo, A.; Koinuma, H.; Segawa, Y. *Appl. Phys. Lett.* **1998**, *72*, 3270.

49. Dong, H.; Liu, Y.; Lu, J.; Chen, Z.; Wang, J.; Zhang, L. *J. Mater. Chem. C* **2013**, *1*, 202.
50. [50] Djurišić, A. B.; Leung, Y. H.; Choy, W. C. H.; Cheah, K. W.; Chan, W. K. *Appl. Phys. Lett.* **2004**, *84*, 2635.
51. Mollow, E. In: *Proceedings of the Photoconductivity Conference*; Breckenridge, R. G.; Wiley: New York, 1954; p 509.
52. Miller, P. H. In: *Proceedings of the Photoconductivity Conference*; Breckenridge, R. G.; Wiley: New York, 1954; p 287.
53. Zhang, D. H. *J. Phys. D: Appl. Phys.* **1995**, *28*, 1273.
54. Studenikin, S. A.; Golego, N.; Cocivera, M. *J. Appl. Phys.* **2000**, *87*, 2413.
55. Sharma, P.; Mansingh, A.; Sreenivas, K. *Appl. Phys. Lett.* **2002**, *80*, 553.
56. Reyes, P. I.; Ku, C.-J.; Duan, Z.; Xu, Y.; Garfunkel, E.; Lu, Y. *Appl. Phys. Lett.* **2012**, *101*, 031118.
57. Studenikin, S. A.; Cocivera, M. *J. Appl. Phys.* **2002**, *91*, 5060.
58. Tamm, J. W.; Ullrich, B.; Qiu, X. G.; Segawa, Y.; Ohtomo, A.; Kawasaki, M.; Koinuma, H. *J. Appl. Phys.* **2000**, *87*, 1844.
59. Heiland, G. *Surf. Sci.* **1969**, *13*, 72.
60. Look, D. C. *Surf. Sci.* **2007**, *601*, 5315.
61. Schmidt, O.; Kiesel, P.; Van de Walle, C. G.; Johnson, N. M.; Nause, J.; Döhler, G. H. *Jpn. J. Appl. Phys.* **2005**, *44*, 7271.
62. Chen, C.-Y.; Chen, M.-W.; Ke, J.-J.; Lin, C.-A.; Retamal, J. R. D.; He, J.-H. *Pure Appl. Chem.* **2010**, *82*, 2055.
63. Mtangi, W.; Nel, J. M.; Auret, F. D.; Chawanda, A.; Diale, M.; Nyamhere, C. *Physica B* **2012**, *407*, 1624.
64. Krusemeyer, H. J. *Phys. Rev.* **1959**, *114*, 655.
65. Heiland, G.; Ibach, H. *Sol. Stat. Commun.* **1966**, *4*, 353.
66. Klingshirn, C. F.; Waag, A.; Hoffmann, A.; Geurts, J. *Zinc Oxide From Fundamental Properties Towards Novel Applications*. Springer-Verlag: Berlin and Heidelberg, 2010.
67. Link, M.; Schreiter, M.; Weber, J.; Gabl, R.; Pitzer, D.; Primig, R.; Wersing, W.; Assouar, M. B.; Elmazria, O. *J. Vac. Sci. Technol. A* **2006**, *24*, 218.
68. Milyutin, E.; Gentil, S.; Mural, P. *J. Appl. Phys.* **2008**, *104*, 084508.
69. Qin, L.; Wang, Q.-M. *J. Appl. Phys.* **2010**, *108*, 104510.
70. Pang, H. F.; Fu, Y. Q.; Hou, R.; Kirk, K.; Hudson, D.; Zu, X. T.; Placido, F. *Ultrasonics* **2013**, *53*, 1264.
71. Lee, Y. E.; Kim, S. G.; Kim, Y. J.; Kim, H. J. *J. Vac. Sci. Technol. A* **1997**, *15*, 1194.
72. Bensmaine, S.; Le Brizoual, L.; Elmazria, O.; Fundenberger, J. J.; Benyoucef, B. *Phys. Status Solidi (a)* **2007**, *204*, 3091.
73. Pang, H. F.; Zhang, G. A.; Tang, Y. L.; Fu, Y. Q.; Wang, L. P.; Zu, X. T.; Placido, F. *Appl. Surf. Sci.* **2012**, *259*, 747.
74. Yanagitani, T.; Morisato, N.; Takayanagi, S.; Matsukawa, M.; Watanabe, Y. *IEEE Trans. Ultrason., Ferroelect., Freq. Contr.* **2011**, *58*, 1062.
75. Zhang, H.; Kosinski, J. A. *IEEE Trans Ultrason Ferroelectr Freq Control* **2012**, *59*, 2831.
76. Yoshino, Y.; Inoue, K.; Takeuchi, M.; Makino, T.; Katayama, Y.; Hata, T. *Vacuum* **2000**, *59*, 403.
77. Novotný, M.; Čížek, J.; Kužel, R.; Bulíř, J.; Lančok, J.; Connolly, J.; McCarthy, E.; Krishnamurthy, S.; Mosnier, J.-P.; Anwand, W.; Brauer, G. *J. Phys. D: Appl. Phys.* **2012**, *45*, 225101.

78. Misra, P.; Kukreja, L. M. *Thin Solid Films* **2005**, *485*, 42.
79. Khranovskyy, V.; Minikayev, R.; Trushkin, S.; Lashkarev, G.; Lazorenko, V.; Grossner, U.; Paszkowicz, W.; Suchocki, A.; Svensson, B. G.; Yakimova, R. *J. Cryst. Growth* **2007**, *308*, 93.
80. Phan, D.-T.; Suh, H.-C.; Chung, G.-S. *Microelectr. Eng.* **2011**, *88*, 105.
81. Kim, J. H.; Kim, E.-M.; Andeen, D.; Thomson, D.; DenBaars, S. P.; Lange, F. F. *Adv. Funct. Mater.* **2007**, *17*, 463.
82. Nakahata, H.; Fujii, S.; Higaki, K.; Hachigo, A.; Kitabayashi, H.; Shikata, S.; Fujimori, N. *Semicond. Sci. Technol.* **2003**, *18*, S96.
83. Pang, H. F.; Garcia-Gancedo, L.; Y. Fu, Q.; Porro, S.; Y. Gu, W.; Luo, J. K.; Zu, X. T.; Placido, F.; Wilson, J. I. B.; Flewitt, A. J.; Milne, W. I. *Phys. Status Solidi (a)* **2013**, *210*, 1575.
84. Garcia-Gancedo, L.; Pedros, J.; Zhu, Z.; Flewitt, A. J.; Milne, W. I.; Luo, J. K.; Ford, C. J. B. *J. Appl. Phys.* **2012**, *112*, 014907.
85. Gulino, A.; Lupo, F.; Fragalà, M. E. *J. Phys. Chem. C* **2008**, *112*, 13869.
86. Tang, K.; Wang, L.; Huang, J.; Xu, R.; Lai, J.; Wang, J.; Min, J.; Shi, W.; Xia, Y. *Plasma Sci. Technol.* **2009**, *11*, 587.
87. Amaike, H.; Hazu, K.; Sawai, Y.; Chichibu, S. F. *Appl. Phys. Express* **2009**, *2*, 105503.
88. Koster, G.; Rijnders, G. J. H. M.; Blank, D. H. A.; Rogalla, H. *Appl. Phys. Lett.* **1999**, *74*, 3729.
89. Hwang, D.-K.; Bang, K.-H.; Jeong, M.-C.; Myoung, J.-M. *J. Cryst. Growth* **2003**, *254*, 449.
90. Hur, T.-B.; Hwang, Y.-H.; Kim, H.-K.; Lee, I. J. *J. Appl. Phys.* **2006**, *99*, 064308.
91. Shi, J.; Wang, X. *J. Phys. Chem. C* **2010**, *114*, 2082.
92. Tsiaoussis, I.; Khranovskyy, V.; Dimitrakopoulos, G. P.; Stoemenos, J.; Yakimova, R.; Pecz, B. *J. Appl. Phys.* **2011**, *109*, 043507.
93. Kim, S.-W.; Fujita, S.; Fujita, S. *Appl. Phys. Lett.* **2002**, *81*, 5036.
94. Lu, J. G.; Ye, Z. Z.; Zhang, Y. Z.; Liang, Q. L.; Fujita, S.; Wang, Z. L. *Appl. Phys. Lett.* **2006**, *89*, 023122.
95. Kluth, O.; Schope, G.; Hüpkens, J.; Agashe, C.; Müller, J.; Rech, B. *Thin Solid Films* **2003**, *442*, 80.
96. Calnan, S.; Upadhyaya, H. M.; Thwaites, M. J.; Tiwari, A. N. *Thin Solid Films* **2007**, *515*(15), 6045–6050.
97. Li, F. M.; Bernhard Bayer, C.; Hofmann, S.; Speakman, S. P.; Ducati, C.; Milne, W. I.; Flewitt, A. J. *Phys. Status Solidi (b)* **2013**, *250*, 957.
98. Bae, S. H.; Lee, S. Y.; Jin, B. J.; Im, S. *Appl. Surf. Sci.* **2000**, *154–155*, 458.
99. Jagadish, C.; Pearton, S. *Zinc Oxide Bulk, Thin Films and Nanostructures*, Elsevier, Oxford, 2006; p 88.
100. Hwang, D.-K.; Oh, M.-S.; Lim, J.-H.; Park, S.-J. *J. Phys. D: Appl. Phys.* **2007**, *40*, R387.
101. Pant, P.; Budai, J. D.; Aggarwal, R.; Narayan, R. J.; Narayan, J. *J. Phys. D: Appl. Phys.* **2009**, *42*, 105409.
102. Yoshida, T.; Tachibana, T.; Maemoto, T.; Sasa, S.; Inoue, M. *Appl. Phys. A* **2010**, *101*, 685.
103. Ohtomo, A.; Tamura, K.; Saikusa, K.; Takahashi, T.; Makino, T.; Segawa, Y.; Koinuma, H.; Kawasaki, M. *Appl. Phys. Lett.* **1999**, *75*, 2635.
104. Tsukazaki, A.; Ohtomo, A.; Yoshida, S.; Kawasaki, M.; Chia, C. H.; Makino, T.; Segawa, Y.; Koida, T.; Chichibu, S. F.; Koinuma, H. *Appl. Phys. Lett.* **2003**, *83*, 2784.

105. Pant, P.; Budai, J. D.; Narayan, J. *Acta Mater.* **2010**, *58*, 1097.
106. Duclere, J.-R.; McLoughlin, C.; Fryar, J.; R. O'Haire, Guilloux-Viry, M.; Meaney, A.; Perrin, A.; McGlynn, E.; Henry, M. O.; Mosnier, J.-P. *Thin Solid Films* **2006**, *500*, 78.
107. Chen, Y. F.; Hong, S.; Ko, H. *Appl. Phys. Lett.* **2000**, *76*, 559.
108. Sha, Z. D.; Wang, J.; Chen, Z. C.; Chen, A. J.; Zhou, Z. Y.; Wu, X. M.; Zhuge, L. J. *Physica E* **2006**, *33*, 263.
109. Wei, X.; Zhao, R.; Shao, M.; Xu, X.; Huang, J. *Nanoscale Res. Lett.* **2013**, *8*, 112.
110. Rogers, D. J.; Look, D. C.; Teherani, F. H.; Minder, K.; Razeghi, M.; Largeau, A.; Demazeau, G. *Phys. Status Solidi (c)* **2008**, *5*, 3084.
111. Yata, S.; Nakashima, Y.; Kobayashi, T. *Thin Solid Films* **2003**, *445*, 259.
112. Kim, T. H.; Nam, S. H.; Park, H. S.; Song, J. K.; Park, S. M. *Appl. Surf. Sci.* **2007**, *253*, 8054.
113. Cho, A. Y.; Arthur, J. R. *Prog. Solid State Chem.* **1975**, *10*, 157.
114. Henini, M. *Molecular Beam Epitaxy: From Research to Mass Production*; Elsevier Inc.: Oxford, 2012; p 369.
115. Opel, M.; Geprags, S.; Althammer, M.; Brenninger, T.; Gross, R. *J. Phys. D: Appl. Phys.* **2014**, *47*, 034002.
116. Zhou, H.; Wang, H.-Q.; Liao, X.-X.; Zhang, Y.; Zheng, J.-C.; Wang, J.-O.; Muhemmed, E.; Qian, H.-J.; Ibrahim, K.; Chen, X.; Zhan, H.; Kang, J. *Nanoscale Res. Lett.* **2012**, *7*, 184.
117. Tsukazaki, A.; Saito, H.; Tamura, K.; Ohtani, M.; Koinuma, H.; Sumiya, M.; Fuke, S.; Fukumura, T.; Kawasaki, M. *Appl. Phys. Lett.* **2002**, *81*, 235.
118. Emanetoglu, N. W.; Gorla, C.; Liu, Y.; Liang, S.; Lu, Y. *Mat. Sci. Semicond. Proc.* **1999**, *2*, 247.
119. Wang, X. Q.; Sun, H. P.; Pan, X. Q. *Appl. Phys. Lett.* **2010**, *97*, 151908.
120. Cho, M. W.; Setiawan, A.; Ko, H. J.; Hong, S. K.; Yao, T. *Semicond. Sci. Technol.* **2005**, *20*, S13.
121. Wang, H.-C.; Liao, C.-H.; Chueh, Y.-L.; Lai, C.-C.; Chou, P.-C.; Ting, S.-Y. *Opt. Mater. Express* **2013**, *3*, 295.
122. Choi, Y. S.; Kang, J. W.; Hwang, D. K.; Park, S. J. *IEEE Trans. Electron. Dev.* **2010**, *57*, 26.
123. Przewdzicka, E.; Wierzbicka, A.; Reszka, A.; Goscinski, K.; Droba, A.; Jakiela, R.; Dobosz, D.; Krajewski, T. A.; Kopalko, K.; Sajkowski, J. M.; Stachowicz, M.; Pietrzyk, M. A.; Kozanecki, A. *J. Phys. D: Appl. Phys.* **2013**, *46*, 035101.
124. Barnes, T. M.; Olsen, K.; Wolden, C. A. *Appl. Phys. Lett.* **2005**, *86*, 112112.
125. Yao, B.; Shen, D. Z.; Zhang, Z. Z.; Wang, X. H.; Wei, Z. P.; Li, B. H.; Lv, Y. M.; Fan, X. W.; Guan, L. X.; Xing, G. Z.; Cong, C. X.; Xie, Y. P. *J. Appl. Phys.* **2006**, *99*, 123510.
126. Wang, L. G.; Zunger, A. *Phys. Rev. Lett.* **2003**, *90*, 256401.
127. Maksimov, O. *Rev. Adv. Mater. Sci.* **2010**, *24*, 26.
128. Jagadish, C.; Pearton, S. *Zinc Oxide Bulk, Thin Films and Nanostructures*, Elsevier: Oxford, 2006; p 448.
129. Janotti, A.; Van de Walle, C. G. *Rep. Prog. Phys.* **2009**, *72*, 126501.
130. Zheng, C. C.; Xu, S. J.; Ning, J. Q.; Bao, W.; Wang, J. F.; Gao, J.; Liu, J. M.; Zhu, J. H.; Liu, X. L. *Semicond. Sci. Technol.* **2012**, *27*, 035008.
131. Kashiwaba, Y.; Haga, K.; Watanabe, H.; Zhang, B. P.; Segawa, Y.; Wakatsuki, K. *Phys. Status Solidi (b)*, **2002**, *229*, 921.
132. Kirchner, C.; Gruber, T.; Reuss, F.; Thonke, K.; Waag, A.; Giessen, C.; Heuken, M. *J. Cryst. Growth* **2003**, *248*, 20.

133. Haga, K.; Abe, S.; Takizawa, Y.; Yubuta, K.; Shishido, T. *J. Phys.: Conf. Ser.* **2013**, *417*, 012059.
134. Jagadish, C.; Pearson, S. *Zinc Oxide Bulk, Thin Films and Nanostructures*. Elsevier: Oxford, 2006; p 448.
135. Hwang, D.-K.; Oh, M.-S.; Lim, J.-H.; Park, S.-J. *J. Phys. D: Appl. Phys.* **2007**, *40*, R387.
136. Liang, H.; Gordon, R. G. *J. Mater. Sci.* **2007**, *42*, 6388.
137. Seki, S.; Onodera, H.; Sekizawa, T.; Sakuma, M.; Haga, K.; Seki, Y.; Sawada, Y.; Shishido, T. *Phys. Status Solidi (c)*, **2010**, *7*, 1565.
138. Hussaina, M.; Hussainb, S. T. *Chem. Eur. J.* **2010**, *1* (2), 96.
139. Nicolay, S.; Benkhaira, M.; Ding, L.; Escarre, J.; Bugnon, G.; Meillaud, F.; Ballif, C. *Solid Energy Mater. Sol. C* **2012**, *105*, 46.
140. Znaidi, L. *Mater. Sci. Eng. B* **2010**, *174*, 18.
141. Viswanatha, R.; Sapra, S.; Satpati, Satyam, P. V.; Dev, B. N.; Sarma, D. D. *J. Mater. Chem.* **2004**, *14*, 661–668.
142. Kubo, R. *J. Phys. Soc. Jpn.* **1962**, *17*, 975.
143. Fonoberov, V. A.; Balandin, A. A. *Phys. Rev. B: Condens. Matter* **2004**, *70*, 195410.
144. Fonoberov, V. A.; Balandin, A. A. *J. Nanoelectron. Optoelectron.* **2006**, *1*, 19.
145. Cheng, H.-M.; Lin, K.-F.; Hsu, H.-C.; Hsieh, W.-F. *Appl. Phys. Lett.* **2006**, *88*, 261909.
146. He, R.; Tsuzuki, T. *J. Am. Ceram. Soc.* **2010**, *93*, 2281.
147. Asok, A.; Gandhi, M. N.; Kulkarni, A. R. *Nanoscale* **2012**, *4*, 4943.
148. Han, L.-L.; Cui, L.; Wang, W.-H.; Wang, J.-L.; Du, X.-W.; *Semicond. Sci. Technol.* **2012**, *27*, 065020.
149. Hsu, S.; Lin, Y. Y.; Huang, S.; Lem, K. W.; Nguyen, D. H.; Lee, D. S. *Nanotechnology* **2013**, *24*, 475102.
150. Sreeja, R.; John, J.; Aneesh, P. M.; Jayaraj, M. K. *Opt. Commun.* **2010**, *283*, 2908.
151. Son, D. I.; Kwon, B. W.; Park, D. H.; Seo, W.-S.; Yi, Y.; Angadi, B.; Lee, C.-L.; Choi, W. K.; *Nature Nanotechnol.* **2012**, *7*, 465.
152. Maikhuri, D.; Purohit, S. P.; Mathur, K. C. *AIP Adv.* **2012**, *2*, 012160.
153. Yuan, Q.; Hein, S.; Misra, R. D. K. *Acta Biomater.* **2010**, *6*, 2732.
154. Forleo, A.; Francioso, L.; Capone, S.; Siciliano, P.; Lommens, P.; Hens, Z. *Sens. Actuators, B* **2010**, *146*, 111.
155. Shao, D.; Sun, X.; Xie, M.; Sun, H.; Lu, F.; George, S. M.; Lian, J.; Sawyer, S. *Mater. Lett.* **2013**, *112*, 165.
156. Tan, S. T.; Sun, X. W.; Zhang, X. H.; Chen, B. J.; Chu, S. J.; Yong, A.; Dong, Z. L.; Hu, X. *J. Cryst. Growth* **2006**, *290*, 518.
157. Zhang, X.; Kobayashi, K.; Tomita, Y.; Maeda, Y.; Kohno, Y. *Phys. Status Solidi (c)* **2013**, *10*, 1576.
158. Lu, J. G.; Ye, Z. Z.; Huang, J. Y.; Zhu, L. P.; Zhao, B. H.; Wang, Z. L.; Fujita, S. *Appl. Phys. Lett.* **2006**, *88*, 063110.
159. Rani, S.; Suri, P.; Shishodia, P. K.; Mehra, R. M. *Sol. Energy Mater. Sol. C* **2008**, *92*, 1639.
160. Zhang, Q.; Dandeneau, C. S.; Zhou, X.; Cao, G. *Adv. Mater.* **2009**, *21*, 4087.
161. Rai, P.; Yu, Y.-T. *Sens. Actuators, B* **2012**, *173*, 58.
162. Xiong, H.-M.; *Adv. Mater.* **2013**, *25*, 5329.
163. Aleshin, A. N.; Shcherbakov, I. P.; Petrov, V. N.; Titkov, A. N. *Org. Electron.* **2011**, *12*, 1285.
164. Hanley, C.; Thurber, A.; Hanna, C.; Punnoose, A.; Zhang, J.; Wingett, D. G. *Nanoscale Res Lett.* **2009**, *4*, 1409.

165. Zhao, M. H.; Wang, Z. L.; Mao, S. X. *Nano Lett.* **2004**, *4*, 587.
166. Chen, C. Q.; Shi, Y.; Zhang, Y. S.; Zhu, J.; Yan, Y. J. *Phys. Rev. Lett.* **2006**, *96*, 075505.
167. Fan, J.; Lee, W.; Hauschild, R.; Alexe, M.; Rhun, G. L.; Scholz, R.; Dadgar, A.; Nielsch, K.; Kalt, H.; Krost, A.; Zacharias, M.; Gosele, U. *Small* **2006**, *2*, 561.
168. Yang, P.; Yan, H.; Mao, S.; Russo, R.; Johnson, J.; Saykally, R.; Morris, N.; Pham, J.; He, R.; Choi, H.-J.; *Adv. Funct. Mater.* **2002**, *12*, 323.
169. Tak, Y.; Yong, K. J.; *J. Phys. Chem. B* **2005**, *109*, 19263.
170. Tian, J.-H.; Hu, J.; Li, S.-S.; Zhang, F.; Liu, J.; Shi, J.; Li, X.; Tian, Z.-Q.; Chen, Y. *Nanotechnology* **2011**, *22*, 245601.
171. Wagner, R. S.; Ellis, W. C. *Appl. Phys. Lett.* **1964**, *4*, 89.
172. Yi, G.-C.; Wang, C.; Park, W. I. *Semicond. Sci. Technol.* **2005**, *20*, S22.
173. Zhu, Z.; Chen, T.-L.; Gu, Y.; Warren, J.; Osgood, R. M. *Chem. Mater.* **2005**, *17*, 4227.
174. Yoo, J.; Hong, Y.-J.; An, S.; Yi, G.-C.; Chon, B.; Joo, T.; Kim, J.-W.; Lee, J.-S. *Appl. Phys. Lett.* **2006**, *89*, 043124.
175. Huang, M. H.; Mao, S.; Feick, H.; Yan, H.; Wu, Y.; Kind, H.; Weber, E.; Russo, R.; Yang, P. *Science* **2001**, *292*, 1897.
176. Banerjee, D.; Rybczynski, J.; Huang, J. Y.; Wang, D. Z.; Kempa, K.; Ren, Z. F. *Appl. Phys. A* **2005**, *80*, 749.
177. Wang, X.; Song, J.; Li, P.; Ryou, J. H.; Dupuis, R. D.; Summers, C. J.; Wang, Z. L. *J. Am. Chem. Soc.* **2005**, *127*, 7920.
178. Fan, H. J.; Zacharias, M. *J. Mater. Sci. Technol.* **2008**, *24*, 589.
179. Wang, X.; Summers, C. J.; Wang, Z. L. *Nano Lett.* **2004**, *4*, 423.
180. Soman, P.; Darnell, M.; Feldman, M. D.; Chen, S. J. *Nanosci. Nanotechnol.* **2011**, *11*, 1.
181. Wen, L.; Wong, K. M.; Fang, Y.; Wu, M. Lei, Y. *J. Mater. Chem.* **2011**, *21*, 7090.
182. Huang, M. H.; Wu, Y.; Feick, H.; Tran, N.; Weber, E.; Yang, P. *Adv. Mater.* **2001**, *13*, 113.
183. Qin, Y.; Yang, R.; Wang, Z. L. *J. Phys. Chem. C* **2008**, *112* (48), 18734.
184. Chik, H.; Liang, J.; Cloutier, S. G.; Kouklin, N.; Xu, J. M. *Appl. Phys. Lett.* **2004**, *84*, 3376.
185. Yi, G.-C. *Semiconductor Nanostructures for Optoelectronic Devices*; Springer: Berlin, 2012; p 12.
186. Miao, L.; Ieda, Y.; Tanemura, S.; Cao, Y. G.; Tanemura, M.; Hayashi, Y.; Toh, S.; Kaneko, K. *Sci. Tech. Adv. Mater.* **2007**, *8*, 443.
187. Park, W. I.; Yi, G. C.; Kim, M. Y.; Pennycook, S. J. *Adv. Mater.* **2002**, *14*, 1841.
188. Greene, L.; Law, M.; Goldberger, J.; Kim, F.; Johnson, J. C.; Zhang, Y. F.; Saykally, R. J.; Yang, P. D. *Angew. Chem., Int. Ed.* **2003**, *42*, 3031.
189. Unalan, H. E.; Hiralal, P.; Rupesinghe, N.; Dalal, S.; Milne, W. I.; Amaratunga, G. A. J. *Nanotechnology* **2008**, *19*, 255608.
190. Baruah, S.; Dutta, J. *Sci. Technol. Adv. Mater.* **2009**, *10*, 013001.
191. Joo, J.; Chow, B. Y.; Prakash, M.; Boyden, E. S.; Jacobson, J. M. *Nat. Mater.* **2011**, *10*, 596.
192. Liu, Z.; Zhu, R.; Zhang, G. *J. Phys. D: Appl. Phys.* **2010**, *43*, 155402.
193. Yeo, J.; Hong, S.; Wanit, M.; Kang, H. W.; Lee, D.; Grigoropoulos, C. P.; Sung, H. J.; Ko, S. H. *Adv. Funct. Mater.* **2013**, *23*, 3316.
194. Mahpeykar, S. M.; Koohsorkhi, J.; Ghafouri-Fard, H. *Nanotechnology* **2012**, *23*, 165602.
195. Wu, G. S.; Xie, T.; Yuan, X. Y.; Li, Y.; Yang, L.; Xiao, Y. H.; Zhang, L. D. *Sol. Stat. Commun.* **2005**, *134*, 485.

196. Htay, M. T.; Tani, Y.; Hashimoto, Y.; Ito, J. *J. Mater. Sci.* **2009**, *20*, 341.
197. Fan, Z.; Dutta, D.; Chien, C.-J.; Chen, H.-Y.; Brown, E. C.; Chang, P.-C.; Lu, J. G. *Appl. Phys. Lett.* **2006**, *89*, 213110.
198. Ramírez, D.; Gómez, H.; Lincot, D. *Electrochim. Acta* **2010**, *55*, 2191.
199. Yang, K. X.; Wang, Z. L. *Appl. Phys. Lett.* **2004**, *84*, 975.
200. Ding, Y.; Wang, Z. L. *J. Phys. Chem. B* **2004**, *108*, 12280.
201. Wang, Z. L. *J. Phys.: Condens. Matter* **2004**, *16*, R829.
202. Wang, Z. L. *J. Mater. Chem.* **2005**, *15*, 1021.
203. Wei, Y.; Ding, Y.; Li, C.; Xu, S.; Ryo, J.-H.; Dupuis, R.; Sood, A. K.; Polla, D. L.; Wang, Z. L. *J. Phys. Chem. C* **2008**, *112* (48), 18935.
204. Zhao, M. H.; Wang, Z. L.; Mao, S. X. *Nano Lett.* **2004**, *4*, 587.
205. Wang, W. Z.; Zeng, B. Q.; Yang, J.; Poudel, B.; Huang, J. Y.; Naughton, M. J.; Ren, Z. F. *Adv. Mater.* **2006**, *18* (24), 3275.
206. Cao, B. Q.; Liu, Z. M.; Xu, H. Y.; Gong, H. B.; Nakamura, D.; Sakai, K.; Higashihata, M.; Okada, T. *CrystEngComm* **2011**, *13*, 4282.
207. Sadek, A. Z.; Choopun, S.; Wlodarski, W.; Ippolito, S. J.; Kalantar-Zadeh, K. *IEEE Sen. J.* **2007**, *7*, 919.
208. Li, F.; Ding, Y.; Gao, P.; Xin, X.; Wang, Z. L. *Angew. Chem.* **2004**, *116*, 5350.
209. Peng, Y.; Xu, A.-W.; Deng, B.; Antonietti, M.; Cölfen, H. *J. Phys. Chem. B* **2006**, *110*, 2988.
210. Hussain, S.; Liu, T.; Kashif, M.; Miao, B.; He, J.; Zeng, W.; Zhang, Y.; Hashim, U.; Pan, F. *Mater. Lett.* **2014**, *118*, 165.
211. Chen, H.; Wu, X.; Gong, L.; Ye, C.; Qu, F.; Shen, G. *Nanoscale Res. Lett.* **2009**, *5*, 570.
212. Xu, C. X.; Sun, X. W.; Dong, Z. L.; Yu, M. B. *Appl. Phys. Lett.* **2004**, *85*, 3878.
213. Ding, G. Q.; Shen, W. Z.; Zheng, M. J.; Fan, D. H. *Appl. Phys. Lett.* **2006**, *88*, 103106.
214. Reiss, P.; Protiere, M.; Li, L. *Small* **2009**, *5* (2), 154.
215. Pugliese, D.; Bella, F.; Cauda, V.; Lamberti, A.; Sacco, A.; Tresso, E.; Bianco, S. *ACS Appl. Mater. Interfaces* **2013**, *5*, 11288.
216. Cheng, C.; Fan, H. J. *Nano Today* **2012**, *7*, 327.
217. Fu, M.; Zhou, J.; Xiao, Q.; Li, B.; Zong, R.; Chen, W.; Zhang, J. *Adv. Mater.* **2006**, *18*, 1001.
218. Chandra, D.; Mridha, S.; Basak, D.; Bhaumik, A. *Chem. Commun.* **2009**, *7*, 2384.
219. Li, Y.; Cai, W.; Duan, G.; Cao, B.; Sun, F.; Lu, F. *J. Colloid Interface Sci.* **2005**, *287*, 634.
220. Polarz, S.; Orlov, A. V.; Schüth, F.; Lu, A. H. *Chemistry* **2007**, *13*, 592.
221. Huang, K.-M.; Ho, C.-L.; Chang, H.-J.; Wu, M.-C. *Nanoscale Res. Lett.* **2013**, *8*, 306.
222. Liu, H. L.; Wu, J. H.; Min, J. H.; Zhang, X. Y.; Kim, Y. K. *Mater. Res. Bull.* **2013**, *48*, 551.
223. Wang, K.; Chen, J. J.; Zeng, Z. M.; Tarr, J.; Zhou, W. L.; Jiang, C. S.; Pern, J.; Mascarenhas, A. *Appl. Phys. Lett.* **2010**, *96*, 123105.
224. Zeng, H.; Cai, W.; Hu, J.; Duan, G.; Liu, P.; Li, Y. *Appl. Phys. Lett.* **2006**, *88*, 171910.
225. Zhou, T.; Lu, M.; Zhang, Z.; Gong, H.; Chin, W. S.; Liu, B. *Adv. Mater.* **2010**, *22*, 403.
226. Zhu, D.; Li, W.; Ma, L.; Lei, Y. *RSC Adv.* **2014**, *4*, 9372.
227. Zhu, Y. F.; Fan, D. H.; Shen, W. Z. *J. Phys. Chem. C* **2008**, *112*, 10402.
228. Saha, S.; Sarkar, S.; Pal, S.; Sarkar, P. *J. Phys. Chem. C* **2013**, *117* (31), 15890.
229. Mayo, D. C.; Marvinney, C. E.; Bililign, E. S.; McBride, J. R.; Mud, R. R.; Haglund, R. F. *Thin Solid Films* **2014**, *553*, 132.
230. Miao, J.; Yang, H. B.; Khoo, S. Y.; Liu, B. *Nanoscale* **2013**, *5*, 11118.
231. Chen, Y.; Wei, L.; Zhang, G.; Jiao, J. *Nanoscale Res Lett.* **2012**, *7* (1), 516.

232. Law, M.; Greene, L. E.; Radenovic, A.; Kuykendall, T.; Liphardt, J.; Yang, P. *J. Phys. Chem. B* **2006**, *110* (45), 22652.
233. Thierry, R.; Perillat-Merceroz, G.; Jouneau, P. H.; Ferret, P.; Feuillet, G. *Nanotechnology* **2012**, *23*, 085705.
234. Yang, P.; Xiao, X.; Li, Y.; Ding, Y.; Qiang, P.; Tan, X.; Mai, W.; Lin, Z.; Wu, W.; Li, T.; Jin, H.; Liu, P.; Zhou, J.; Wong, C. P.; Wang, Z. L. *ACS Nano* **2013**, *7* (3), 2617.
235. Elias, J.; Levy-Clement, C.; Bechelany, M.; Michler, J.; Wang, G.-Y.; Wang, Z.; Philippe, L. *Adv. Mater.* **2010**, *22*, 1607.
236. Li, C.; Li, G.; Shen, C.; Hui, C.; Tian, J.; Du, S.; Zhang, Z.; Gao, H.-J. *Nanoscale* **2010**, *2*, 2557.
237. Shi, R.; Yang, P.; Wang, J.; Zhang, A.; Zhu, Y.; Cao, Y.; Ma, Q. *CrystEngComm* **2012**, *14*, 5996.
238. McPeak, K. M.; Le, T. P.; Britton, N. G.; Nickolov, Z. S.; Elabd, Y. A.; Baxter, J. B. *Langmuir* **2011**, *27*, 3672.
239. Zhang, H.; Yang, D.; Ma, X.; Ji, Y.; J. Xu, Que, D. *Nanotechnology* **2004**, *15*, 622.
240. Pan, A.; Yu, R.; Xie, S.; Zhang, Z.; Jin, C.; Zou, B. *J. Cryst. Growth* **2005**, *282*, 165.
241. Baxter, J. B.; Aydil, E. S. *Appl. Phys. Lett.* **2005**, *86*, 053114.
242. Jiang, C. Y.; Sun, X. W.; Lo, G. Q.; Kwong, D. L.; Wang, J. X. *Appl. Phys. Lett.* **2007**, *90*, 263501.
243. He, F.-Q.; Zhao, Y.-P. *Appl. Phys. Lett.* **2006**, *88*, 193113.
244. Lao, J. Y.; Wen, J. G.; Ren, Z. F. *Nano Lett.* **2002**, *2* (11), 1287.
245. Fan, H. J.; Scholz, R.; Kolb, F. M.; Zacharias, M. *Appl. Phys. Lett.* **2004**, *85*, 4142.
246. Xu, X.; Wu, M.; Asoro, M.; Ferreira, P. J.; Fan, D. L. *Cryst. Growth Des.* **2012**, *12* (10), 4829.
247. Deng, J.; Yu, B.; Lou, Z.; Wang, L.; Wang, R.; Zhang, T. *Sens. Actuators, B* **2013**, *184*, 21.
248. Ko, S. H.; Lee, D.; Kang, H. W.; Nam, K. H.; Yeo, J. Y.; Hong, S. J.; Grigoropoulos, C. P.; Sung, H. J. *Nano Lett.* **2011**, *11*, 666.
249. Yeo, L. Y.; Friend, J. R. *Annu. Rev. Fluid Mech.* **2014**, *46*, 379.
250. Büyükköse, S.; Vratzov, B.; van der Veen, J.; Santos, P. V.; van der Wiel, W. R. *Appl. Phys. Lett.* **2013**, *102*, 013112.
251. Smith, W. R.; Gerard, H. M.; Collins, J. H.; Reeder, T. M.; Shaw, H. J. *IEEE Trans. Microwave Theory Technol.* **1969**, *17*, 856.
252. Du, X. Y.; Fu, Y. Q.; Tan, S. C.; Luo, J. K.; Flewitt, A. J.; Milne, W. I.; Lee, D. S.; Park, N. M.; Park, J.; Choi, Y. J.; Kim, S. H.; Maeng, S. *Appl. Phys. Lett.* **2008**, *93*, 094105.
253. Mitsuyu, T.; Ono, S.; Wasa, K. *J. Appl. Phys.* **1980**, *51*, 2464.
254. Mortet, V.; Williams, O. A.; Haenen, K. *Phys. Status Solidi (a)* **2008**, *205*, 1009.
255. Luo, J. K.; Fu, Y. Q.; Milne, S. B.; Le, H. R.; Williams, J. A.; Spearing, S. M.; Flewitt, A. J.; Milne, W. I. *J. Micromech. Microeng.* **2007**, *17*, S147.
256. Fujii, S. *Phys. Status Solidi (a)* **2011**, *208*, 1072.
257. Fujii, S.; Shikata, S.; Uemura, T.; Nakahata, H.; Harima, H. *IEEE Trans. Ultrason. Ferroelectr. Freq. Control.* **2005**, *52*, 1817.
258. Campbell, C. K. *Proc. IEEE*, **1989**, *77* (10), 1453–1484.
259. Jin, H.; Zhou, J.; He, X.; Wang, W.; Guo, H.; Dong, S.; Wang, D.; Xu, Y.; Geng, J.; Luo, J. K.; Milne, W. I. *Sci. Rep.* **2013**, *3*, 2140.
260. Ippolito, S. J.; Kandasamy, S.; Kalantar-Zadeh, K.; Wlodarski, W.; Galatsis, K.; Kiria-kidis, G.; Katsarakis, N.; Suche, M. *Sens. Actuators, B* **2005**, *111–112*, 207.
261. Pang, H.-F.; Fu, Y.-Q.; Li, Z.-J.; Li, Y.-F.; Placido, F.; Walton, A. J.; Zu, X.-T. *Sens. Actuators A* **2013**, *193*, 87.

262. Singh, D.; Narasimulu, A. A.; Garcia-Gancedo, L.; Fu, Y. Q.; Hasan, T.; Lin, S. S.; Geng, J.; Shao, G.; Luo, J. K. *J. Mater. Chem. C* **2013**, *1*, 2525.
263. Grudkowski, T. W.; Black, J. F.; Reeder, T. M.; Cullen, D. E.; Wagner, R. A. *Appl. Phys. Lett.* **1980**, *37*, 993.
264. Hashimoto, K.; *RF Bulk Acoustic Wave Filters for Communications*; Artech House: Norwood, MA/London, 2009; p 52.
265. Qin, L.; Chen, Q.; Cheng, H.; Wang, Q. M. *IEEE Trans Ultrason. Ferroelectr. Freq. Control* **2010**, *57* (8), 1840.
266. Link, M.; Schreiter, M.; Weber, J.; Primig, R.; Pitzer, D.; Gabl, R. *IEEE Trans Ultrason. Ferroelectr. Freq. Control* **2006**, *53* (2), 492.
267. Chen, D.; Wang, J.; Xu, Y.; Li, D.; Zhang, L.; Liu, W. J. *Micromech. Microeng.* **2013**, *23*, 095032.
268. García-Gancedo, L.; Pedrós, J.; Iborra, E.; Clement, M.; Zhao, X. B.; Olivares, J.; Capilla, J.; Luo, J. K.; Lu, J. R.; Milne, W. I.; Flewitt, A. J. *Sens. Actuators, B* **2013**, *183*, 136.
269. Shung, K. K. *Diagnostic Ultrasound: Imaging and Blood Flow Measurements*; CRC Press: Boca Raton, FL, 2006, Vol 3; p 46.
270. Hashimoto, K.; Suzuki, H.; Yamamoto, M.; Yamaguchi, M. *Proc. IEEE Ultrason. Symp.* **1989**, 339–342.
271. Yamamoto, M.; Hashimoto, K.; Rajendran, V.; Yamaguchi, M. *Jpn. J. Appl. Phys.* **1990**, *29*, 53.
272. Cannata, J. M.; Williams, J. A.; Zhou, Q. F.; Sun, L.; Shung, K. K.; Yu, H.; Kim, E. S. *J. Appl. Phys.* **2008**, *103* (8), 084109.
273. Feng, G.-H.; Sharp, C. C.; Zhou, Q. F.; Pang, W.; Kim, E. S.; Shung, K. K. *J. Micromech. Microeng.* **2005**, *15*, 586.
274. Martin, P. M.; Good, M. S.; Johnston, J. W.; Posakony, G. J.; Bond, L. J.; Crawford, S. L. *Thin Solid Films* **2000**, *379* (1–2), 253.
275. Zhou, Q.; Lau, S.; Wu, D.; Shung, K. K. *Prog. Mater. Sci.* **2011**, *56*, 139.
276. Ito, Y.; Kushida, K.; Sugawara, K.; Takeuchi, H. *IEEE Trans Ultrason. Ferroelectr. Freq. Control* **1995**, *42*, 316.
277. Jen, C.-K.; Sreenivas, K.; Sayer, M. *J. Acoust. Soc. Am.* **1988**, *84*, 26.
278. Pang, H. F.; Fu, Y. Q.; Hou, R.; Kirk, K. J.; Hutson, D.; Zu, X. T.; Placido, F. *Ultrasonics* **2013**, *53*, 1264.
279. Yanagitani, T.; Morisato, N.; Takayanagi, S.; Matsukawa, M.; Watanabe, Y. *IEEE Trans. Ultrason. Ferroelectr. Freq. Control* **2011**, *58*, 1062.
280. Ding, X.; Li, P.; Lin, S.-C. S.; Stratton, Z. S.; Nama, N.; Guo, F.; Slotcavage, D.; Mao, X.; Shi, J.; Costanzo, F.; Huang, T. J. *Lab Chip* **2013**, *13*, 3626.
281. Du, X. Y.; Fu, Y. Q.; Luo, J. K.; Flewitt, A. J.; Milne, W. I. *J. Appl. Phys.* **2009**, *105*, 024508.
282. Alghane, M.; Chen, B. X.; Fu, Y. Q.; Li, Y.; Desmulliez, M. P. Y.; Mohammed, M. I.; Walton, A. *J. Phys. Rev. E* **2012**, *86*, 056304.
283. Alghane, M.; Chen, B. X.; Fu, Y. Q.; Li, Y.; Luo, J. K.; Walton, A. J. *J. Micromech. Microeng.* **2011**, *21*, 015005.
284. Pang, H. F.; Fu, Y. Q.; Garcia-Gancedo, L.; Porro, S.; Luo, J. K.; Placido, F.; Wilson, B.; Flewitt, A. J.; Milne, W. I.; Zu, X. T. *Microfluids Nanofluids* **2013**, *15*, 377.
285. Fu, Y. Q.; Li, Y.; Zhao, C.; Placido, F.; Walton, A. *J. Appl. Phys. Lett.* **2012**, *101*, 194101.
286. Reboud, J.; Bourquin, Y.; Wilson, R.; Pall, G. S.; Jiwaji, M.; Pitt, A. R.; Graham, A.; Waters, A. P.; Cooper, J. M. *PNAS* **2012**, *109* (38), 15162.

287. Hoummady, M.; Campitelli, A.; Wlodarski, W. *Smart Mater. Struct.* **1997**, *6*, 647.
288. Sadek, A.; Wlodarski, W.; Li, Y.; Yu, W.; Yu, X.; Kalantar-Zadeh, K.; Li, X. *Thin Solid Films* **2007**, *515*, 8705.
289. Tasaltin, C.; Ebeoglu, M. A.; Ozturk, Z. Z. *Sensors* **2012**, *12*, 12006.
290. Ippolito, S. J.; Kandasamy, S.; Kalantar-Zadeh, K.; Wlodarski, W. *Sens. Actuators, B* **2005**, *108*, 553.
291. Ippolito, S. J.; Ponzoni, A.; Kalantar-Zadeh, K.; Wlodarski, W.; Comini, E.; Faglia, G.; Sberveglieri, G. *Sens. Actuators, B* **2006**, *117*, 442.
292. Huang, F.-C.; Chen, Y.-Y.; Wu, T.-T. *Nanotechnology* **2009**, *20*, 065501.
293. Jakubik, W. P. *Thin Solid Films* **2007**, *515*, 8345.
294. Nagai, H.; Kawai, S.; Ito, O.; Oizumi, T.; Tsuji, T.; Takeda, N.; Yamanaka, K. Possibility for Sub-ppm Hydrogen Detection with the Ball SAW Sensor. In: *The 20th International Congress on Acoustics*, Sydney, Australia, 23–27 August, 2010.
295. García-González, D. L. *Aparicio R. Grasas y Aceites*, *53. Fasc.* **2002**, *1*, 96.
296. Dasgupta, D.; Sreenivas, K. *J. Appl. Phys.* **2011**, *110*, 044502.
297. Emanetoglu, N. W.; Zhu, J.; Chen, Y.; Zhong, J.; Chen, Y.; Lu, Y. *Appl. Phys. Lett.* **2004**, *85*, 3702.
298. Wei, C.-L.; Chen, Y.-C.; Cheng, C.-C.; Kao, K.-S.; Cheng, D.-L.; Cheng, P.-S. *Thin Solid Films* **2010**, *518*, 3059.
299. Wu, T.-T.; Wang, W.-S.; Chou, T.-H.; Chen, Y.-Y. *J. Acoust. Soc. Am.* **2008**, *123*, 3377.
300. Sharma, P.; Sreenivas, K. *Appl. Phys. Lett.* **2003**, *83*, 3617.
301. Kumar, S.; Sharma, P.; Sreenivas, K. *Semicond., Sci. Technol.* **2005**, *20*, L27.
302. Phan, T.; Chung, G.-S. *Curr. Appl. Phys.* **2012**, *12*, 521–524.
303. Kumar, S.; Kim, G.-H.; Sreenivas, K.; Tandon, R. P. *J. Electroceram.* **2009**, *22*, 198.
304. Peng, W.; He, Y.; Wen, C.; Ma, K. *Sens. Actuators A* **2012**, *184*, 34.
305. Phan, D.-T.; Chung, G.-S. *Curr. Appl. Phys.* **2012**, *12*, 210.
306. Wang, W.-S.; Wu, T.-T.; Chou, T.-H.; Chen, Y.-Y. *Nanotechnology* **2009**, *20*, 135503.
307. Chivukula, V.; Ciplis, D.; Shur, M.; Dutta, P. *Appl. Phys. Lett.* **2010**, *96*, 233512.
308. Water, W.; Jhao, R.-Y.; Ji, L.-W.; Fang, T.-H.; Chen, S.-E. *Sens. Actuators A* **2010**, *161*, 6.
309. Chu, S. Y.; Water, W.; Liaw, J. T. *Ultrasonics* **2003**, *4*, 133.
310. Chang, R.-C.; Chu, S.-Y.; Hong, C.-S.; Chuang, Y.-T. *Thin Solid Films* **2006**, *498*, 146.
311. Länge, K.; Rapp, B. E.; Rapp, M. *Anal. Bioanal. Chem.* **2008**, *391*, 1509.
312. Voiculescu, I.; Nordin, A. N. *Biosens. Bioelectron.* **2012**, *33*, 1.
313. Rocha-Gaso, M.-I.; March-Iborra, C.; Montoya-Baides, Á.; Arnau-Vives, A. *Sensors* **2009**, *9*, 5740.
314. Kalantar-Zadeh, K.; Wlodarski, W.; Chen, Y. Y.; Fry, B. N.; Galatsis, K. *Sens. Actuators, B* **2003**, *91*, 143.
315. Krishnamoorthy, S.; Iliadis, A. A.; Bei, T.; Chrousos, G. P. *Biosens. Bioelectron.* **2008**, *24*, 313.
316. Luo, J.; Luo, P.; Xie, M.; Du, K.; Zhao, B.; Pan, F.; Fan, P.; Zeng, F.; Zhang, D.; Zheng, Z.; Liang, G. *Biosens. Bioelectron.* **2013**, *49*, 512.
317. Tigli, O.; Bivona, L.; Berg, P.; Zaghloul, M. E. *IEEE Trans. Biomed. Circuits Syst.* **2010**, *4*, 62.
318. Nirschl, M.; Schreiter, M.; Voros, J. *Sens. Actuators, A* **2011**, *165*, 415.
319. Lin, R.-C.; Chen, Y.-C.; Chang, W.-T.; Cheng, C.-C.; Kao, K.-S. *Sens. Actuators, A* **2008**, *147*, 425.
320. Mai, L.; Kim, D.-H.; Yim, M.; Yoon, G. *Microw. Opt. Technol. Lett.* **2004**, *42*, 505.
321. Johnston, M. L.; Kymissis, I.; Shepard, K. L. *IEEE Sensors J.* **2010**, *10*, 1042.

- 322. Nirschl, M.; Schreiter, M.; Vörös, J. *Sens. Actuators, A* **2011**, *165*, 415.
- 323. Link, M.; Weber, J.; Schreiter, M.; Wersing, W.; Elmazria, O. Alnot, P. *Sens. Actuators, B* **2007**, *121*, 372.
- 324. Garcia-Gancedo, L.; Pedros, J.; Zhao, X. B.; Ashle, G. M.; Flewitt, A. J.; Milne, W. I.; Ford, C. J. B.; Lu, J. R.; Luo, J. K. *Biosens. Bioelectron.* **2012**, *38*, 369.
- 325. Pottigari, S. S.; Kwon, J. W. *IEEE International Conference on Solid-State Sensors, Actuators and Microsystems*, Denver, CO, June 21–25, 2009; pp 156–159.
- 326. Zhao, X.; Pan, F.; Ashley, G. M.; Garcia-Gancedo, J.; Luo, J.; Flewitt, A. J.; Milne, W. I.; Lu, J. R. *Sens. Actuators, B* **2014**, *190*, 946.
- 327. Chen, Y.; Reyes, P. I.; Duan, Z.; Saraf, G.; Wittstruck, R.; Lu, Y.; Taratula, O.; Galoppini, E. *J. Electron. Mater.* **2009**, *38* (8), 1605–1611.
- 328. Weber, J.; Albers, W. M.; Tuppurainen, J.; Link, M.; Gabl, R.; Wersing, W.; Schreiter, M. *Sens. Actuators, A* **2006**, *128*, 84.
- 329. Xu, W.; Zhang, X.; Choi, S.; Chae, J. *J. Microelectromech. S* **2011**, *20*, 213.
- 330. Chen, D.; Wang, J.; Xu, Y.; Li, D. *Sens. Actuators, B* **2012**, *171–172*, 1081.
- 331. Wang, Z.; Qiu, X.; Shi, J.; Yu, H. *J. Electrochem. Soc.* **2012**, *159*, J13.
- 332. Chen, D.; Wang, J.; Li, D.; Liu, Y.; Song, H.; Li, Q. *J. Micromech. Microeng.* **2011**, *21*, 085017.
- 333. Chen, D.; Wang, J.; Liu, Q.; Xu, Y.; Li, D.; Liu, Y. *J. Micromech. Microeng.* **2011**, *21*, 115018.
- 334. Wang, Z.; Qiu, X.; Chen, S. J.; Pang, W.; Zhang, H.; Shi, J.; Yu, H. *Thin Solid Films* **2011**, *519*, 6144.
- 335. Qiu, X.; Tang, R.; Zhu, J.; Oiler, J.; Yu, C.; Wang, Z.; Yu, H. *Sens. Actuators, B* **2011**, *151*, 360.